UC Davis

UC Davis Electronic Theses and Dissertations

Title

Investigating the dust effects on the modulation of large-scale circulations and cloud activities over North Africa and the Eastern Atlantic Ocean using a fully coupled regional atmosphere-dust-ocean model

Permalink

https://escholarship.org/uc/item/4m48b6cj

Author

Wang, Tai-Jyun

Publication Date

2022

Peer reviewed|Thesis/dissertation

eScholarship.org Powered by the California Digital Library
University of California

Investigating the dust effects on the modulation of large-scale circulations and cloud activities over North Africa and the Eastern Atlantic Ocean using a fully coupled regional atmosphere-dust-ocean model

By

TAI-JYUN WANG
THESIS

Submitted in partial satisfaction of the requirements for the degree of

MASTER OF SCIENCE

in

Atmospheric Science

in the

OFFICE OF GRADUATE STUDIES

of the

UNIVERSITY OF CALIFORNIA

DAVIS

Approved:

Shu-Hua Chen, Chair

Terrence R. Nathan

Paul A. Ullrich

Committee in Charge

2022

Abstract

This study examines how dust-cloud-radiation interactions modulate large-scale circulations and reduce meteorological variable errors over North Africa and the Atlantic Ocean using a fully coupled atmosphere-dust-ocean model. Two one-month numerical experiments in June 2020 are conducted: activation (DON) and deactivation (DOFF) of dust-radiation-cloud interactions. Model results show that the dust effects correct large-scale circulations that greatly reduce the biases and root mean square errors (RMSEs) of meteorological variables in the atmosphere. The improvement on these errors is mainly attributed to the improvement of the temperature and energy fields, which modify the vertical instability and the wind field through the thermal wind relation. The intensity and the northward shift of the African easterly jet (AEJ) are corrected by the gradient of the dust heating. As a result, the maximum RMSE of 650-hPa wind speed is reduced by 90% over the major error region. In addition, the 750-hPa temperature RMSE is improved by as much as 91%. Near the surface, the maximum RMSEs of 10-m wind, 2-m temperature, and 2-m moisture are reduced by 83%, 91%, and 72%, respectively. The Intertropical Discontinuity (ITD) zone and the Intertropical Convergence Zone (ITCZ) are shifted to the north due to the intensified southwesterly monsoonal flow over this region. These near-surface wind changes are mainly caused by the dust radiative heating, which creates a low-pressure anomaly and a convergent cyclonic circulation anomaly underneath the dust plume. The influence of dust on cloud activities, in particular those initiated to the south of the ITD, and cloud-relevant variables (e.g., wind) are also examined. Because of the dust-induced low-level circulation, when a dust plume propagates along the ITD region, the area-mean south-northerly wind (12ºN to 24ºN and 5ºW to 15ºE) becomes weaker (i.e., northerly flow) as the dust plume enters the region, and becomes stronger (i.e., southerly) as the

dust plume exits the region. Compared to DOFF, dust enhances the northward moisture transport at this ITD region when stronger southerly winds occur, and as a result, storms have a higher likelihood to develop stronger and farther into the north.

Introduction

Dust plays an important role on Earth. It can affect human activities, energy budget, weather, and climate change near dust source regions and beyond. Dust scatters and absorbs incoming shortwave radiation. In general, the net dust-shortwave radiation interaction warms the air temperature at the upper part of a dust plume and cools air below due to energy attenuation by dust (Chen et al., 2010; Pérez et al., 2006). On the other hand, dust absorbs, scatters, and emits longwave radiation, heating the air at the lower part of the dust plume and cooling the dust plume above. During the daytime, dust overall warms the upper part of the dust plume, dominated by the dust-shortwave radiation interaction, while it cools or warms the lower dust plume depending on dust distribution and dominant process (i.e., dust-shortwave or dust-longwave radiation interaction). At night when only the longwave radiation operates, dust warms the lower part of the dust plume and cools the upper part of the plume (Choobari et al., 2014). As a result, the dust direct radiative effect can modify the environmental temperature, the stability, and the vertical shear through the thermal wind relation. These will influence large-scale circulations and cloud activities, in which the latter is the dust semi-direct effect.

In addition to the dust direct and semi-direct effects, dust also alters cloud optical properties and lifecycle by serving as cloud condensation nuclei (CCN) and ice nuclei (IN), resulting in the modification of the energy budget (Karydis et al., 2011), the so-called dust indirect effect (Fan et al., 2009; Gettelman & Morrison, 2015; Shi et al., 2014). Dust particles are good IN. The dust-IN effect is considered through different heterogeneous ice nucleation processes, including deposition nucleation, condensation freezing, immersion freezing and contact freezing (Field et al., 2006). Since the heterogeneous nucleation processes produce more ice-phase hydrometeors and thus additional latent heat is released above the freezing levels but below the homogeneous nucleation

levels (~40ºC; DeMott et al., 1998), they can help invigorate the storm's intensity and produce more precipitation (Paukert et al., 2017). For the dust-CCN effect alone, dust can increase the cloud number concentration but with smaller cloud droplet sizes, which can prolong the lifetime of the clouds (Ross et al., 2003; Zhang et al., 2007). In addition, these clouds will scatter and reflect more solar shortwave radiation (Romakkaniemi et al., 2012). Dust is hydrophobic whose hygroscopicity parameter (kappa) is in general very small (~0.05; Koehler et al., 2009), but for severe dust storms near the source regions, the dust-CCN effect can still be important due to high dust concentrations.

The Sahara Desert is the world's largest hot desert. The desert is located in the subtropical ridge region, where the upper-tropospheric air descends, causing the warming and drying of the lower atmosphere, and discouraging cloud formation. The Sahara emits the largest amount of dust, about 790–840 million tons annually (Querol et al., 2019). These dust plumes occur episodically during the entire year but are maximized in the warm season. Through the dust-radiation-cloud interactions, Saharan dust can influence an array of weather systems, covering different spatiotemporal scales over North Africa and the tropical Atlantic Ocean and beyond (Dunion & Velden, 2004).

The African easterly jet (AEJ) is formed, via the thermal wind relation, due to the warmer air to the north in the desert and colder to the south. Studies have shown that Saharan dust can influence the AEJ (Bangalath & Stenchikov, 2015; Bercos-Hickey et al., 2020; Chen et al., 2015). The heating by dust on the Saharan air (warm) side enhances meridional temperature gradient and thus strengthens the AEJ. In consequence, African easterly waves (AEWs) that are generated due to the instability of AEJ are expected to be influenced by the dust effects as well (Bercos-Hickey et al., 2017; Grogan et al., 2016, 2019; Nathan et al., 2017, 2019; Schwendike & Jones, 2010).

Grogan et al., (2016) used idealized simulations to examine how dust influences AEWs. They show that the growth rates of AEWs are enhanced by the dust radiative effect by 5-20%. Moreover, when the dust is transported westward, it can interact with AEWs and slow their westward propagation speed (Nathan et al., 2017). During the incipient growth phase of AEWs, the directions of the dust transports which move westward to the Atlantic ocean are controlled by the background dust gradient. Nathan et al. (2019) found that the eddy (AEWs) can transport the largest amount of the dust at where the largest background dust gradient meets a critical surface, the surface where the wave propagation speed is the same as the background mean flow.

Saharan dust can also modify precipitation systems such as mesoscale convective systems (MCSs) (Huang et al., 2019; Liu et al., 2019; Martínez & Chaboureau, 2018) and those associated with West African Monsoon (WAM) (Nicholson, 2009; Zhao et al., 2011) and Intertropical Convergence Zone (ITCZ) (Evans et al., 2020; Nicholson, 2009; Wilcox et al., 2010). Zhoa et al. (2011) showed that precipitation associated with the WAM weather systems is reduced up to 0.14 mm/h in the late afternoon and increased up to 0.04 mm/h in the early morning. They claimed that this is because the energy budget is changed by the dust and atmospheric diabatic heating so that the instability is increased during the day and decreased during the night. Huang et al. (2019) compared the impact of the dust-radiation versus the dust-cloud effect on the development of an MCS over North Africa. They show that the dust-radiation effect has a far greater impact on MCS's development than the dust-cloud effect. While the former effect invigorates the MCS development, the latter can further enhance development through heterogeneous freezing processes (mainly the immersion freezing process). As a result, it increases the precipitation amount of the system (Huang et al., 2019). Wilcox et al. (2010) used 9 years of the NASA Terra satellite observation data and NCEP/NCAR reanalysis from 2000 to 2008 to show that dust increases the precipitation

at the northern side of ITCZ and reduces the amount at the southern side, shifting the ITCZ convection northward. They explained that it is due to the collocation of the increased precipitation with the dust-enhanced mid-level positive vorticity and the easterly wind shear south of the jet core at 10ºN to 12ºN, resulting from the intensification of the 850-hPa temperature gradient by dust (i.e., the thermal wind relation). In this study, we propose a different mechanism to explain why ITCZ is shifted northward through the analysis of dust radiative heating.

Dust modifies the energy budget not only in the atmosphere but also in the upper ocean. Studies have shown that dust can reduce surface energy fluxes, and change upper ocean characteristics, sea surface temperature (SST), and near-surface meteorological variables, modulating air-sea interactions (Chen et al., 2021; Evan et al., 2008; Jordan et al., 2018; Strong et al., 2015). Strong et al. (2015) used a global model to assess the influence of dust on the tropical Atlantic Ocean and climate in West Africa by conducting two simulations, one using strong absorbing dust (ABS) and the other using strong scattering dust (SCT). In the ABS simulations, the upper-ocean heat content is decreased due to the dust effect, whereas in the SCT simulations dust increases the upper-ocean heat content. Jordan et al. (2018) used the same model to study the dust effects with versus without the coupling of the atmosphere and ocean to further investigate how dust-induced changes in air-sea interactions feedback to the ITCZ rainfall. In the atmosphere-ocean coupled simulations, rainfall is decreased by dust over the eastern Atlantic Ocean because dust cools SST and reduces surface latent heat flux. On the contrary, in the uncoupled simulations (i.e., no feedback from dust-induced ocean changes), dust increases the rainfall over the eastern Atlantic Ocean. These opposite results inform us that dust-induced SST and surface energy flux changes have important feedback on dust-already-modified weather systems in the atmosphere,

pointing out the importance of using a fully coupled model for such studies. Thus, a fully coupled atmosphere-dust-ocean model is used to conduct our numerical simulations.

Chen, et al. (2021) examined the dust influences on upper-ocean characteristics and air-sea interactions over the Tropical North Atlantic Ocean using a high-resolution coupled regional model. They used the warm season in 2015 for the study. Their results show that dust cools the SST at the western African coastal regions but warms SST at the southwestern portion of the dust plume toward the western Atlantic Ocean. They find that dust influences the air-sea interactions not only through the changes of the surface downward radiation fluxes by dust but also by dust-induced changes in low-level meteorology variables. They show that dust creates a negative sea level pressure anomaly underneath the dust plume, which drives a cyclonic circulation anomaly. The circulation anomaly contributes to the changes of the upper-ocean mixed layer depth change and latent and sensible heat fluxes.

This study is an extension of Chen et al. (2021). Their study mainly examines how dust modifies air-sea interactions and near surface meteorological variables, but not variables in the free atmosphere, which will be examined here. In addition, the impact of dust on weather systems and large-scale circulations through different processes has been examined in many studies (Chen et al., 2021; Choobari et al., 2014; Dunion & Velden, 2004; Zhang et al., 2007). But, how these dust-induced processes improve model simulations has not been presented systematically and will be quantitatively examined in this study.

The paper is organized as follows. Section 2 describes the WRF-ROMS-DUST (WRD) model, experimental designs, and data used. Section 3 evaluates the model performance and the modification of large-scale circulations and cloud activity by dust. The summary and discussion will be included in Section 4.

1. Numerical model and experiment design

2.1 Numerical model description

In this study, we use a fully coupled WRF-ROMS-DUST (WRD) model. The WRD model, integrates two existing models: the Coupled Ocean–Atmosphere–Wave–Sediment Transport (COAWST) model by Warner et al., (2008, 2010) and the Weather Research and Forecasting (WRF) dust model by Chen et al. (2010, 2015). The COAWST model couples with the WRF model (Skamarock et al., 2008), the Regional Ocean Modeling System (ROMS, Shchepetkin & McWilliams, 2005), and the Simulating WAves Nearshore (SWAN) wave model with the Sediment Transport Model capability (Warner et al., 2010). All model components can capture the scale from a few meters to thousands of kilometers. ROMS provides sea surface temperature (SST) to WRF, while WRF feeds surface energy flux and wind stress back to ROMS. In this study, the wave component is turned off.

Chen et al. (2010, 2015) implemented the dust-continuity equation and dust-physics processes in the WRF. Five size bins with median dust radii of 0.25, 0.5, 1, 2, and 4 μm are used in this model. The dust-radiation interaction is added to the Fu-Liou-Gu (FLG) radiation scheme (Gu et al., 2010, 2011) in the WRF-Dust model (Chen et al., 2021). There are 18 aerosol types in the FLG scheme, including 5 different sizes of mineral dust. The flux form of the dust continuity equation is written as follows:

$$\frac{\partial \mu\gamma}{\partial t} = \nabla \cdot \vec{V}\mu\gamma + \gamma_{pbl} + \gamma_{con} + \gamma_{mic} + S_\gamma + E_\gamma \qquad (1)$$

In (1), $\mu = (p_s - p_t)$ is the column mass and is equal to the hydrostatic pressure difference between the model surface (p_s) and the model top (p_t); γ is the dust mixing ratio (kg/kg); γ_{pbl} is

dust subgrid boundary layer mixing; γ_{con} is dust subgrid cumulus mixing; γ_{mic} is the dust sink/source term for microphysical processes such as dust being activated as CCN and wet scavenged by clouds; S_γ represents dust sedimentation and dry deposition processes, and E_γ represents dust emission from the surface. In this study, we assume that dust emission occurs only in any grid where the land surface is barren, the soil volumetric is less than 0.2, and the 10-m wind speed exceeds 6.5 m/s. Further details of the dust model can be found in Chen et al. (2015).

To include dust-cloud interaction, in this study we choose a two-moment microphysics scheme (Cheng et al., 2010) which was implemented in the WRF dust model by Chen et al. (2015) and tested by Huang et al. (2019). In this scheme, dust can act both as IN and CCN. For the ice phase, dust heterogeneous ice nucleation processes (J.-P. Chen et al., 2008; Hoose et al., 2010) are included. For the liquid phase, an adsorption process, in which uncoated mineral dust particles can be activated as CCN (Kumar et al., 2011b, 2011a; Navea et al., 2010), is included. Based on J. P. Chen et al. (2013), the critical radius for dust-CCN activation and the equilibrium size of activated cloud drops are used.

2.2 Experimental designs

The central objective of this study is to evaluate the impact of dust-cloud-radiation interactions on cloud activities over North Africa and the eastern Atlantic Ocean. Chen et al. (2021) have only shown the importance of dust in modifying air-sea interactions. However, how dust modulates cloud activities over this region is an unanswered question in their study. In addition, dust can modify SST change, which will have feedback to the atmosphere. What is the contribution of dust-induced SST change to cloud modulation by dust? Both will be examined in this study. To accomplish these, two 1-month numerical experiments, from 1 to 30 June 2020, are conducted as

shown in Table 1. The experiments are as follows: activation of dust-radiation-cloud interactions (DON) and deactivation of dust-radiation-cloud interactions (DOFF). When analyzing the results, the first half month data are discarded due to the model's spin up and only the last 15 days data are used for average.

In the model, we use two domains for the atmosphere (i.e., WRF) and one domain for the ocean (i.e., ROMS) (Figure 1). The first domain uses 12 km resolution, covering approximately 75^{o} W to 39^{o} E and 10^{o} S to 45^{o} N. The initial and boundary conditions of two experiments are from 6-hourly NCEP FNL (Final) Operational Global Analysis data for the atmosphere and 1/12^{o} Hybrid Coordinate Ocean Model (HYCOM) analysis (updated every 10 days) for the ocean. To include the dust effect, the Cheng et al. two-moment microphysics scheme (Cheng et al., 2010; Huang et al., 2019), the FLG radiation scheme (Gu et al., 2010, 2011, p. 20), the Kain-Fritsch (KF) cumulus scheme (Kain, 2004) and the Medium Range Forecast (MRF) boundary layer scheme (Hong & Pan, 1996) are chosen for the numerical experiments. The Generic Length Scale (GLS) vertical mixing scheme is used (Umlauf & Burchard, 2003) for the ocean.

Table 1. *The design of the two numerical experiments. Model integration will span from 1 to 30 June 2020.*

Experiments	*Description*
DON	The WRD model is used for 1-month integration, starting from 1 to 30 June 2020. Dust-radiation-cloud interactions are activated.
DOFF	Same as DON, except dust-radiation-cloud interactions are deactivated.

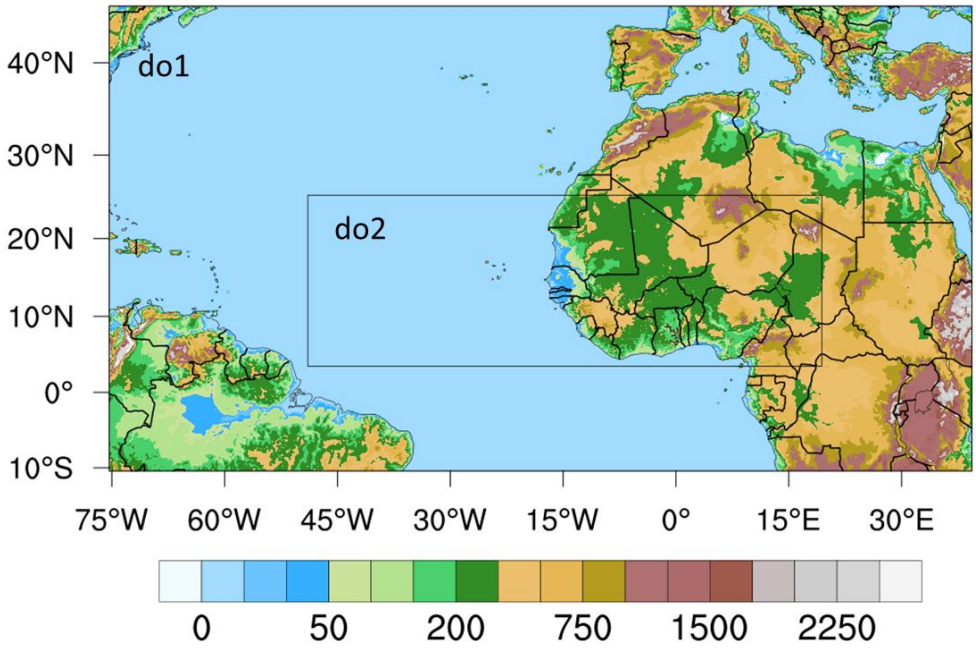

Figure 1. *Domain configuration for the study from 1 to 30 June 2020. Domain 1 (d01) is the parent domain with a horizontal resolution of 12 km. Domain 2 (d02) is the child domain with a resolution of 4 km.*

2. Simulation Results and Error Statistics

Chen et al. (2021) investigated how Saharan dust modulates air-sea interactions through different dust-induced mechanisms over the North Atlantic Ocean. In this follow-up study, we will examine and quantify how Saharan dust improves meteorological variables and large-scale circulations in the atmosphere, such as AEJ, if it indeed occurs. Before we examine the improvement by dust, we will first evaluate model dust since it plays an important role in DON results.

Due to the model spin-up issue, only data from 16 to 30 June 2020 (15 days) at 3-h intervals will be used for analysis unless otherwise mentioned. The model results will be compared with reanalysis data and observations.

3.1 Evaluation of model dust simulation

Dust is the only type of aerosol included in the WRD model. Since there are no systemic dust observations that cover a wide area for a long time available for the model dust verification, we will need to rely on satellite data, which in general includes all types of aerosols. Saharan dust is the dominant aerosol over the Tropical North Atlantic Ocean during the warm season. Thus, aerosol optical depth (AOD) observations from satellites can be still used to evaluate our dust simulation result, though model AOD is most likely underestimated over the ocean due to the additional marine aerosols in observed AOD.

Figure 2 shows the 15-day average AOD from DON and the Visible Infrared Imaging Radiometer Suite (VIIRS) instrument onboard the Satellite Suomi NPP. The Level 2 deep blue VIIRS AOD data (6 km × 6 km resolution) at 550 nm is used. Note that since observed AOD are available mainly around 1200 UTC, model AOD during the same period is used in the plot. Overall, the AOD patterns between the observation and DON are comparable over the Saharan dust plume region. For example, the model captures the high AOD values outside the coast of Mauritania (~1.5) and over West Chad and East Niger (~2; ~17°N and 16°E). However, the model overestimates AOD in three regions: along the northwestern coast of North Africa, along 18ºN in the southern desert, and the wide coverage of high AOD in Chad. As a result, the model AOD gradient (or heating gradient) will be too high near these regions. On the other hand, the model underestimates AOD over the northeast Mauritania (the northeast-southwest yellow band in the northwestern desert in Figure 2a).

Over the ocean, AOD is underestimated in the model in part due to model errors (dust sizes, dust emission parameterization, etc.) and the neglect of sea salt aerosol. Moreover, observed AOD south of the equator is mainly from biomass burning and this is not included in the WRD model.

Although the modeled dust is far from perfect, the simulated AOD is in reasonable agreement with the observation in terms of the pattern and magnitude. Thus, the influence of dust on atmospheric large-scale circulations and meteorological variables can be reasonably evaluated. We note that the dust parameterizations in the WRD model are not ideal and there is room for improvement. Thus, this study intends to evaluate the first order of the dust effects on the improvement of large-scale circulations and meteorological variables.

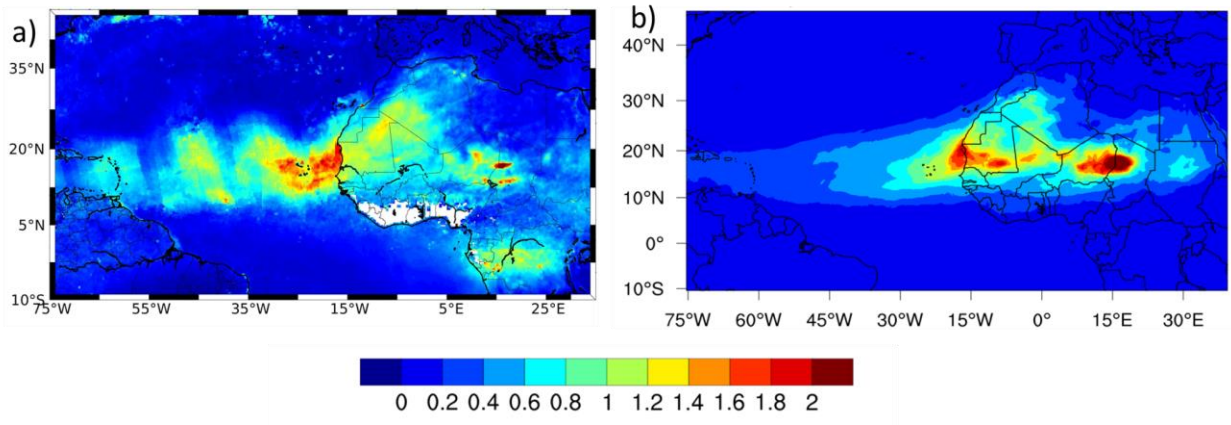

Figure 2. *The 15-day mean aerosol optical depth (AOD; unitless) at the wavelength of 550 nm from (a) observations and (b) DON. The observed AOD are from the VIIRS instrument onboard the Satellite Suomi NPP.*

3.2 Dust effects on simulated meteorological variables and large-scale circulations - error statistics

In this subsection, we examine the influence of dust-radiation-cloud interactions on simulated meteorological variables and large-scale circulations by comparing model results between DON and DOFF against FNL reanalysis. The biases and root mean square errors (RMSEs) of

meteorological variables in the free atmosphere and near the surface will be quantified, and how dust influences large-scale circulations that help reduce errors will be explained.

Note that the total dust or AOD from DON is superimposed onto DOFF figures as a reference of the dust plume location for discussion since the major bias and RMSE are often related to the dust. As a reminder, all plotted fields are 15-day averages from 16 to 30 June 2020.

a. 750 and 900-hPa temperatures

Figure 3 shows the 750-hPa temperature field from observations and two experiments. The temperature at 750-hPa is analyzed since this is a typical level where the heating by Saharan dust is more evident in the warm season. Compared with reanalysis, the 750-hPa in DOFF is generally too cold. Without the dust effects (i.e., DOFF), the 750-hPa temperature in most areas in domain 1 has cold biases (blue shading), except for two small positively-biased regions located at the southern edge of the dust plume over the land: one at ~ 10ºN and 15ºW and the other at ~ 10ºN and 38ºW. Large biases and RMSE are present in the northwestern half of the desert and are collocated with the dust ridge. The maximum cold bias is about 4.5 K at about 22ºN and 12ºE (Figure 4).

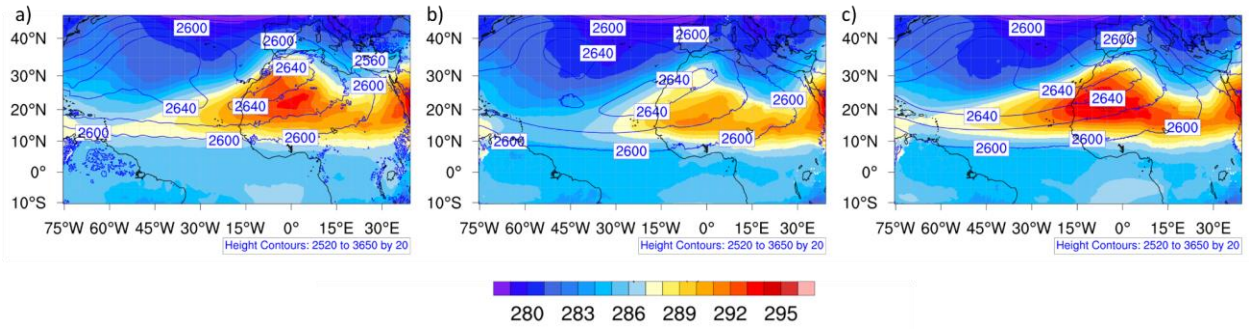

Figure 3. *The mean temperature (K; shading) and geopotential height (m; contours) at 750 hPa for (a) FNL reanalysis, (b) DOFF, and (c) DON from 16 to 30 June 2020.*

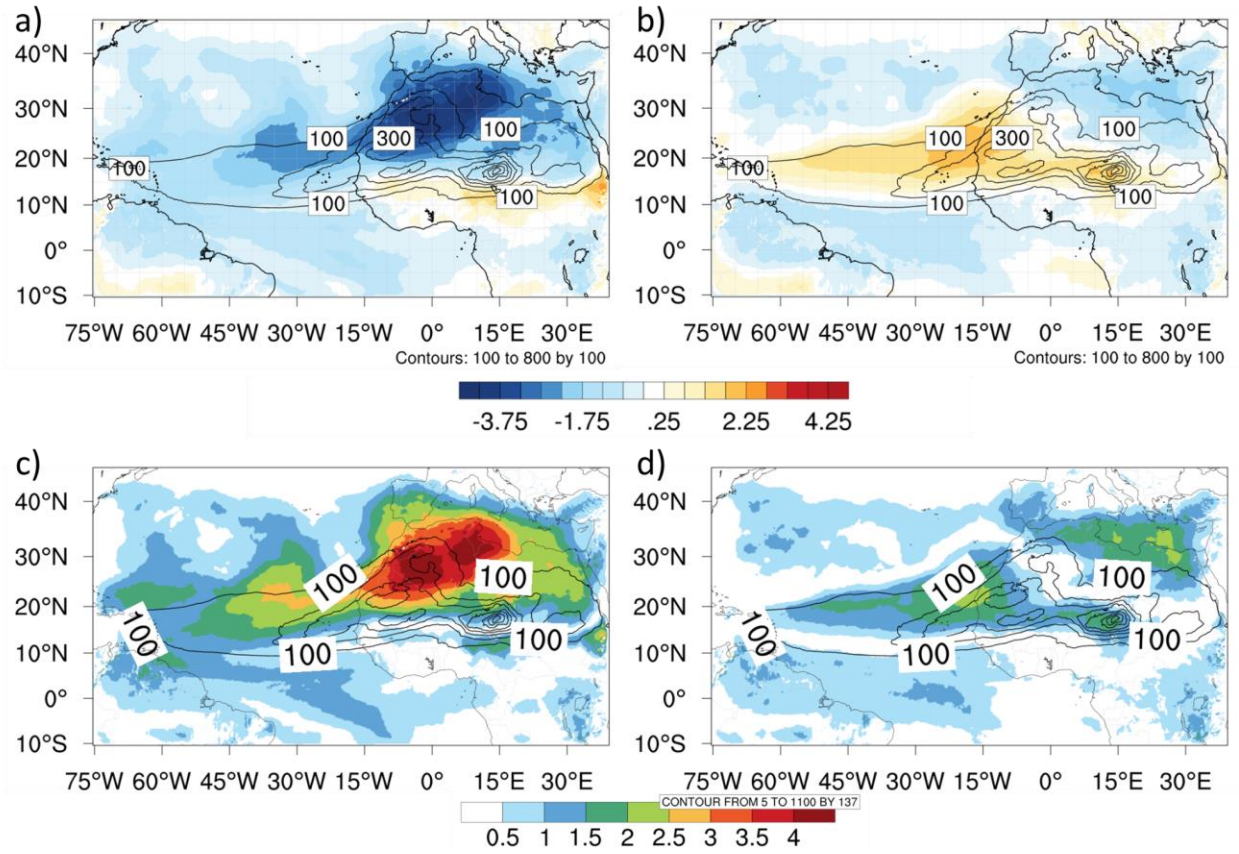

Figure 4. *The (a, b) mean bias and (c, d) RMSE of 750-hPa temperature for DOFF (left) and DON (right) against reanalysis data from 16 to 30 June 2020. The black contours are the total dust amount (μg/kg) from DON for reference.*

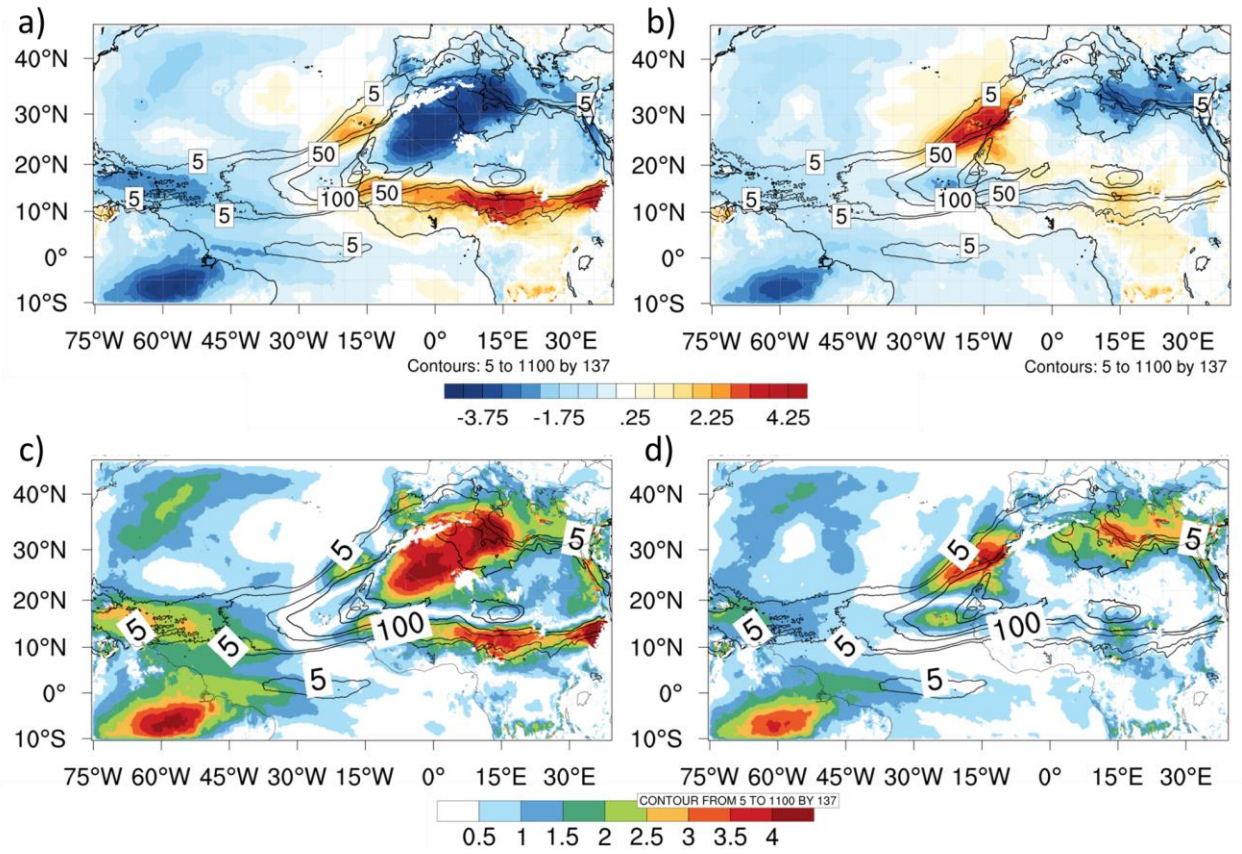

Figure 5. *The same as Figure 4, except for 900 hPa.*

Over the ocean, the maximum cold bias in DOFF is at the northern half of DON's dust plume east of 45ºW. The cold bias becomes smaller away from the dust source region when the dust concentration is small. The cold bias further extends to the outside of the dust plume with smaller magnitudes.

Similar to 750-hPa, the temperature errors at 900-hPa in DOFF have a similar pattern of cold biases and RMSEs at the northwestern half of the desert with comparable magnitudes (Figure 4 versus Figure 5). However, the 750-hPa temperature error that extends from the northwestern coast to 40ºW along the northern side of the dust plume disappears at 900-hPa. But additional negative biases and larger RMSEs appear on the western side of domain 1 between 10ºN to 20ºN and 48ºW to 75ºW at the 900-hPa level. The 900-hPa warm bias (about 3 to 5 K) and large RMSEs become

apparent south of the intertropical discontinuity (ITD) zone (about 10 to 15ºN), a zone where the dry warmer Saharan air in the north meets the colder moist air in the south. In addition, a small warm bias with a maximum of ~2.5K is present outside the northwestern coastal line at ~25ºN.

Because of the dust radiative heating, the heating effect compensates for the cold bias in DOFF. Compared with reanalysis, the 750-hPa warm temperature pattern in DON becomes much more realistic than in DOFF as shown in Figure 3. For example, the Saharan temperature ridge at ~20ºN is better captured in DON and so is the westward extension of the warm air to the Atlantic Ocean (Figure 3b versus Figure 3c). However, the temperature correction by dust is overdone (i.e., becomes warm bias) west of the prime meridian over most of the dust plume region (Figure 4). Additional warm bias is found in the Lake Chad region (~15ºN and 15ºE), where the dust concentration is the highest and is very likely overstimulated by the model. As a result of the dust effects, the temperature bias and RMSE in DON resemble the dust plume shape quite well over certain areas (Figure 4a versus Figure 4b and Figure 4c versus Figure 4d). The errors partly created by dust are due to the inaccurate dust emission, size distribution, transport, and/or optical properties. Even though the dust overcorrects the cold bias, the RMSE of the 750-hPa temperature is still improved at the northwestern half of the desert (~26ºN, 1ºW) from 4.6 K to 0.4 K (91%). Outside the dust plume, the RMSE and the cold biases are slightly reduced.

Unlike DOFF, in DON the patterns of temperature errors at 900-hPa are quite different from those at 750-hPa (Figure 4b versus Figure 5b and Figure 4d versus Figure 5d) due to different competition between dust-shortwave and dust-longwave interactions at these two levels and model error. The cold bias and RMSE of 900-hPa temperature over the maximum dust plume region in the desert are greatly reduced by dust heating (Figure 5a versus Figure 5b and Figure 5c versus Figure 5d). The maximum RMSE is reduced from 4.8 K to 0.4 K (~92%) by dust, and the

overcorrection of the cold bias does not occur at this level. The dust also fixes the cold bias far downstream of the dust plume (9ºN to 20ºN and 32ºW to 75ºW).

Not only is the dust capable of correcting the cold bias over the desert, but it can also correct the warm bias to the south of the ITD zone at 900-hPa. The RMSE is also greatly reduced there. Three possible reasons are proposed. First, the location of the ITD zone is corrected by dust by shifting northward, i.e., by retreating warm air northward (more discussion is given in the next section). Second, the dust concentration is very low or zero in the lower atmosphere over this region (figure not shown). Thus, the radiation energy change at low levels is dominated by the shortwave radiation attenuated by dust above, while the dust-longwave heating is almost nil (i.e., the net cooling effect). Third, the development of the deep convective clouds (DCC) associated with ITCZ is enhanced by dust (to be discussed in section 3.3), and more effectively attenuates shortwave radiation reaching the low levels (e.g., 900-hPa). However, the dust worsens the warm bias over the coastal region and the maximum RMSE is almost doubled by dust. The reasons need further investigation.

In summary, the dust-radiation effect plays an important role in reducing temperature errors over the dust plume region, including the southward extension to the south of the ITD, where the 900-hPa warm temperature bias is located. We found that the temperature errors in DOFF are mainly caused by dust-induced biases. Thus, once the biases are corrected by dust, the RMSEs are greatly reduced. But the temperature at some locations and levels are overcorrected. This is due to inaccurate dust simulations contributed by the dust parameterizations in the model, such as dust emission, size distribution, optical properties, and transport. Further improvements in dust parameterizations in the model are needed in the future.

b. 650-hPa wind

Figure 6 shows the 650-hPa wind speeds and vectors from reanalysis and two experiments. The winds at 650-hPa are commonly analyzed since this is where the maximum AEJ locates in the warm season. Compared to reanalysis, the intensity, location, and westward extension of the AEJ are apparently better captured in DON than in DOFF.

In DOFF, the AEJ is too weak and short. The high wind (> 15 m/s) is limited to the east of 20ºW, and the jet is located too much southward (Figure 6a versus 6b). Large biases and errors are found over North Africa and the tropical and subtropical North Atlantic Ocean (Figures 7a and 7c). The AEJ intensity is underestimated by 8.7 m/s (blue shading; Figure 7a versus 7b). Conversely, the easterly wind is too strong south of the AEJ and the overestimation extends to the south of the equator. The magnitude of the maximum bias reaches as high as 8.8 m/s. In a few tests, we found that compared to reanalysis, the overestimation of winds in this region is potentially due to the PBL scheme used in WRD simulations. We are currently implementing the dust in the YSU PBL scheme (Hong et al., 2006). To the north of the jet between 20ºN to 40 ºN, where 650-hPa winds are relatively weak, there exist both the positive and negative biases.

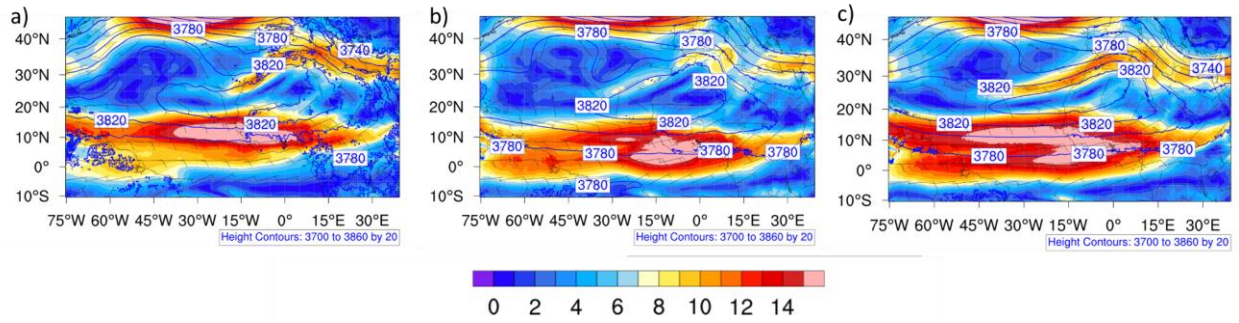

Figure 6. *The mean wind speeds (m/s), vectors, and geopotential height (m) at 650-hPa from (a) FNL reanalysis, (b) DOFF, and (c) DON.*

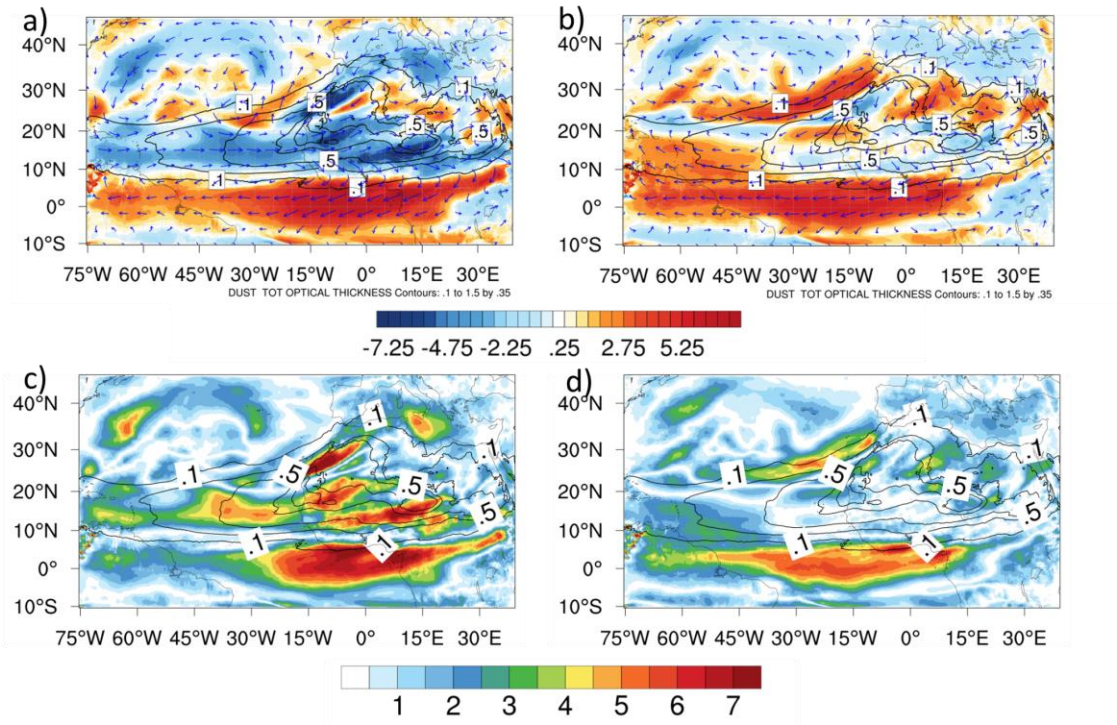

Figure 7. *The mean (a, b) bias and (c, d) RMSE of 650-hPa wind speed and vectors for DOFF (left) and DON (right) against reanalysis data from 16 to 30 June 2020. The black contours are AOD from DON for reference.*

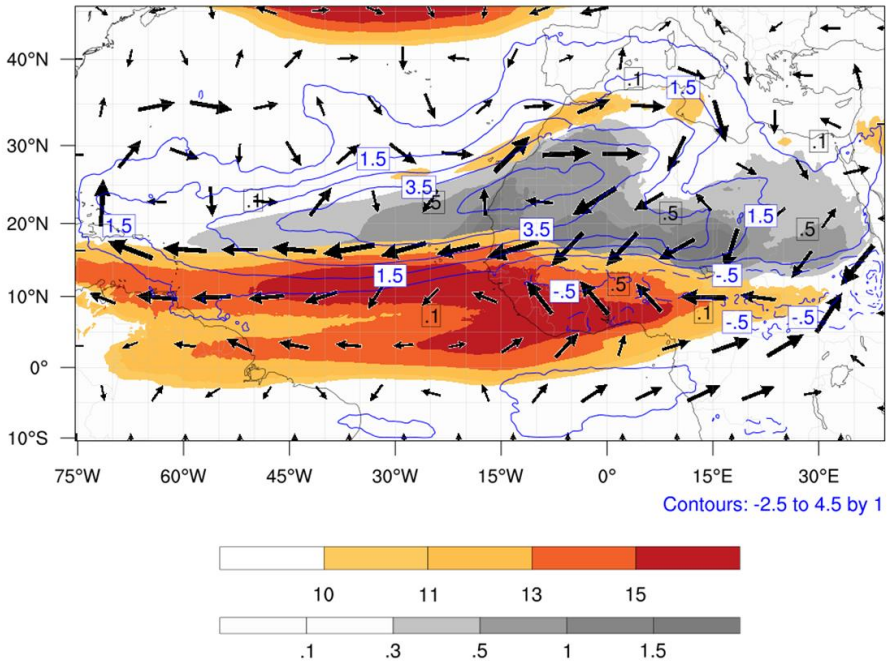

Figure 8. *The 650-hPa mean wind speed for DON. Gray shading represents the AOD from DON. The blue contours represent the difference of 750-hPa temperature between DON and DOFF (DON - DOFF). Black arrows are wind vector differences between DON and DOFF.*

After adding the dust-radiation-cloud effects (i.e., DON), the AEJ extends from the northwestern North African coast to the ocean, though the extension is much further west. The jet in DON is shifted northward, which is more consistent with the reanalysis (Figure 6b versus Figure 6c). The northward shift is because the AEJ is corrected by the gradient of the dust heating, which is located to the north of the jet in DOFF (Figure 8).

Statistics show that DON significantly reduces the biases and RMSEs in DOFF over the major error regions east of 35ºW (Figures 7b and 7d), where a cyclonic circulation bias surrounding the dust plume region is present in DOFF. This is because the heating by dust induces a clockwise vertical wind shear anomaly through the thermal wind relation and results in a mean anticyclonic flow anomaly surrounding the dust plume. Since the low-level winds are usually weaker and the change by dust is smaller, the modification in the vertical shear mainly reflects the wind changes in the middle levels (Figure 8). The maximum RMSE is reduced by 90% from 7.8 m/s to 0.8 m/s over this region.

As in the temperature fields, additional wind errors are also introduced by dust (Figure 7a versus 7b and 7c versus 7d). While winds are improved over and near the dust source region, the westerly wind bias becomes easterly at the downstream of the dust plume over the western Atlantic Ocean (~15ºN, 60ºW in Figure 7b). This is probably because the simulated dust becomes worse over this region as the error of the dust simulation continues growing in time when moving westward after the long-range transport, overwhelming the benefit of including the dust effects.

The inclusion of the dust effects also amends the bias and RMSE to the south of the maximum AEJ, though the improvement is less prominent (Figure 7d). The major improvement is still at the eastern side toward the dust source region, while the error grows again toward the western Atlantic

Ocean away from the dust sources. The maximum RMSE over this region is reduced by 62% from 5.4 m/s to 2.1 m/s. To the north of the AEJ, the RMSE of 650-hPa wind is improved but the bias at the northern edge of the dust plume (~25ºN) becomes larger because of the dust effects.

In general, over and near the dust source regions, the biases and RMSEs of 650-hPa winds are clearly improved due to the temperature gradient changes by dust, which modifies the wind field through the thermal wind relation. However, away from the dust source region, as the model error grows in time, the wind biases and RMSEs in DON become slightly larger than DOFF and the biases often change signs (i.e., overcorrected). The dust long-range transport and dust-radiation-cloud interactions require further improvement in order to reduce wind errors away from the source regions.

c. Near surface variables

Figure 9 shows 15-day averaged 10-m wind, 2-m temperature (T2), and 2-m moisture (Q2) from reanalysis, DOFF, and DON. Compared to reanalysis, the strong northeasterly trade winds over the southern and southeastern branch of the subtropical high are narrower and weaker and shifted southward in DOFF than in DON (Figure 9a versus 9b and 9c). Consequently, the ITCZ over the ocean is also shifted southward since the northeasterly flow becomes too strong at the 9ºN in DOFF (Figures 9b and 9c). The southerly equatorial flow is too weak in both DON and DOFF and is very likely due to the neglect of biomass-burning aerosols south of the equator. Compared to DOFF, the pattern of the Saharan warm air near the surface (T2) is nicely captured by DON (Figure 9f) and the maximum 2-m temperature (T2) is about ~312K (DON) over the desert which is similar to the reanalysis (Figure 9d versus Figure 9f). Compared to reanalysis, the Saharan desert

warm and dry air is expanded further south in DOFF than in DON. The moist zones over the ITCZ between 0ºN to 10ºN and along the western North Atlantic are nicely reproduced in DON.

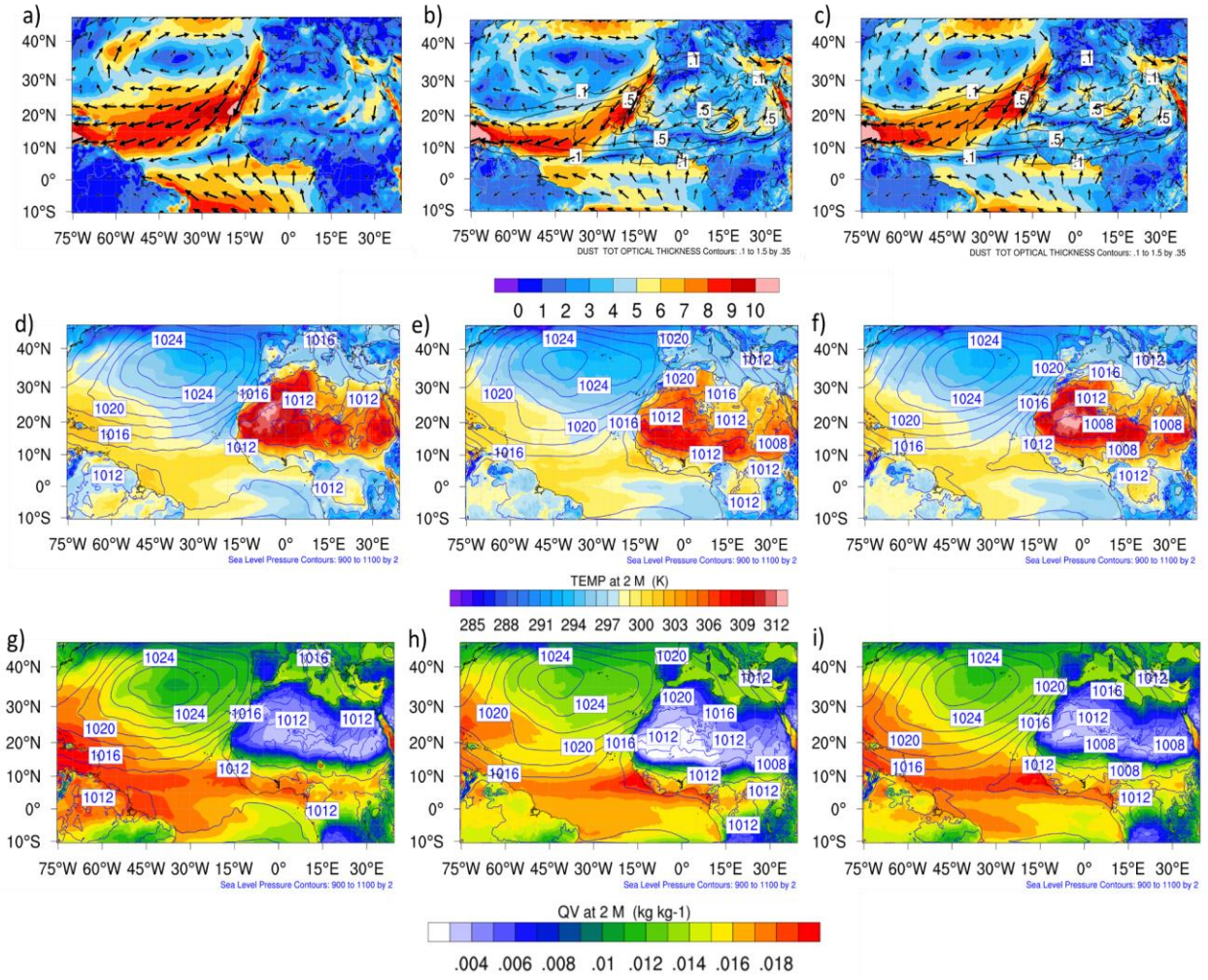

Figure 9. *(a-c) The mean 10-m wind speed (shading; m/s) and vectors, (d-f) 2-m temperature (T2), and (g-i) 2-m water vapor mixing ratio (Q2) for (left) FNL reanalysis, (middle) DOFF, and (right) DON from 16 to 30 June 2020.*

The large errors and biases of near surface variables associated with synoptic-scale circulations due to the neglect of the dust effects (i.e., DOFF) can be more clearly seen in error statistics. Significantly weak 10-m trade winds (part of subtropical high) are shown in DOFF (Figure 10a), and the maximum RMSE is about 4.1 m/s at 20 ºN and 33ºE (Figure 10c). Over North Africa, a dipole pattern of 10-m wind speed bias (positive to the north and negative to the

south) is present between 10ºN to 20ºN in DOFF. The dipole-pattern wind bias is introduced by the southward shift of the ITD zone, resulting from relatively weaker southwesterly monsoonal flow (blue shading) and stronger northeasterly Harmattan flow (red shading) over this region.

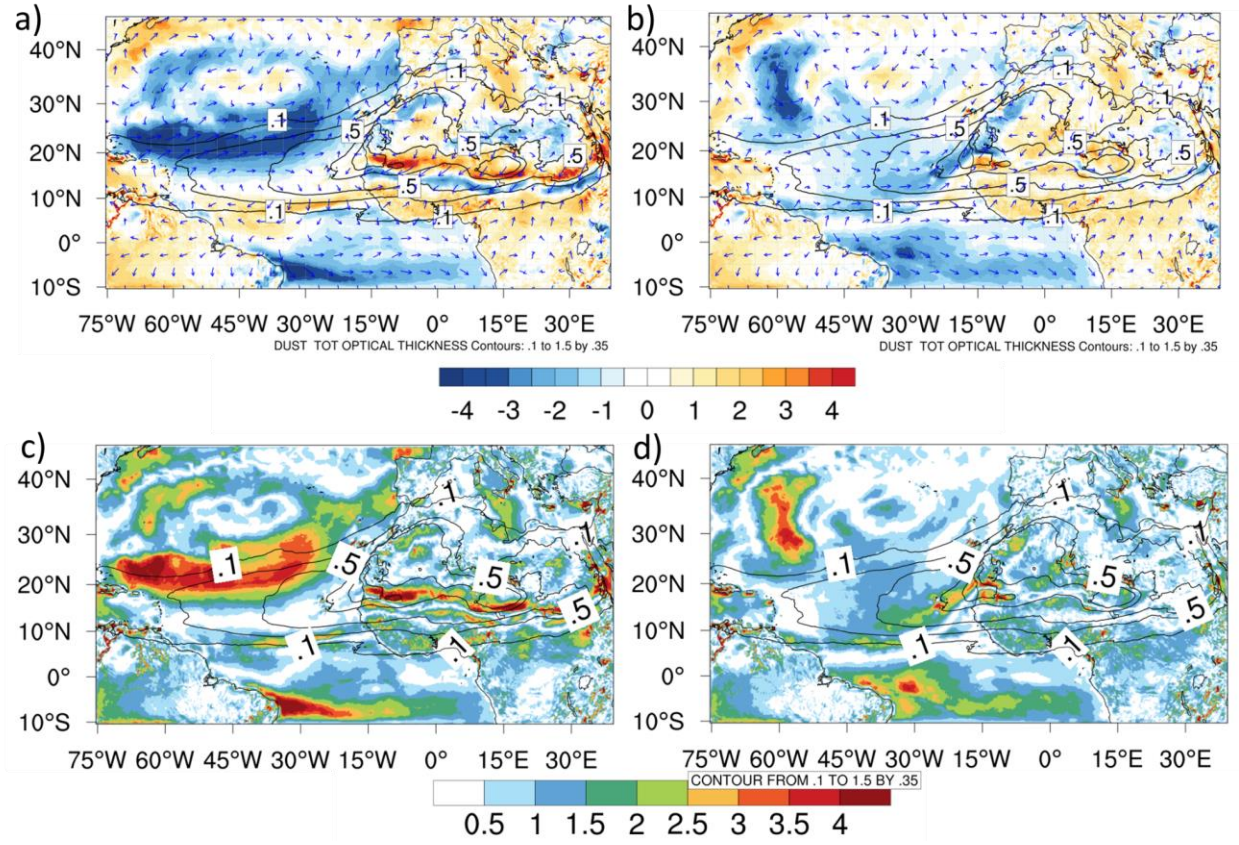

Figure 10. *The 15-day mean (a, b) bias and (c, d) RMSE of 10-m wind for (left) DOFF and (right) DON against reanalysis data from 16 to 30 June 2020. The black contours are AOD from DON for reference.*

For T2 errors in DOFF, large cold biases and RMSEs are present in the Sahara Desert with the maximum magnitude of the negative bias about 5.1 K (Figure 11a and Figure 11c). At the south of the desert, warm bias is present between 5ºN to 13ºN and 19ºW to 38ºE with a maximum of ~4.6 K. This is in part due to the warm desert air shifting southward in DOFF. Compared to the errors over the land, the T2 biases over the ocean are much smaller (-0.5K ~ -2K) due to smaller surface response in ocean than in land, in addition to a smaller dust concentration over the ocean.

Small warm biases exist along the western African coast, underneath the dust plume over the eastern Atlantic Ocean, while cold biases exist downstream and outside of the dust plume.

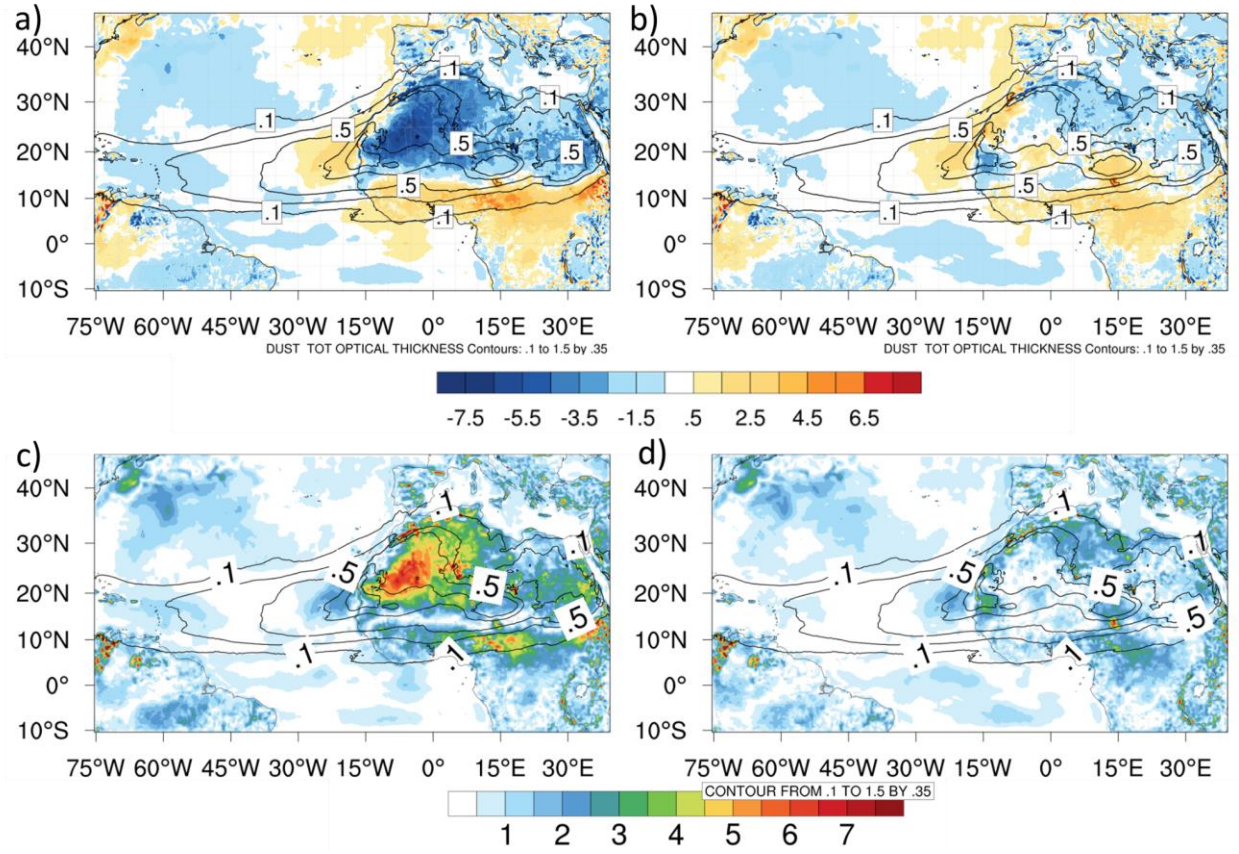

Figure 11. *The 15-day mean (a, b) bias and (c, d) RMSE of 2-m temperature for (left) DOFF and (right) DON against reanalysis data from 16 to 30 June 2020. The black contours are AOD from DON for reference.*

For Q2 errors in DOFF, an eye-catching dry bias band and errors are present at ~13ºN over the land with the maximum magnitude of 7.9 g/kg (Figure 12a and Figure 12c). Similar to T2 discussed earlier, this is because of the southward shift of the ITD zone that expands warm and dry desert air further south when the dust effects are neglected. Over the ocean, a small wet bias is found outside the dust plume along the coastal region of western North Africa, while a small dry

bias is found underneath the dust plume and toward the western Atlantic Ocean, similar to T2 bias patterns over the ocean.

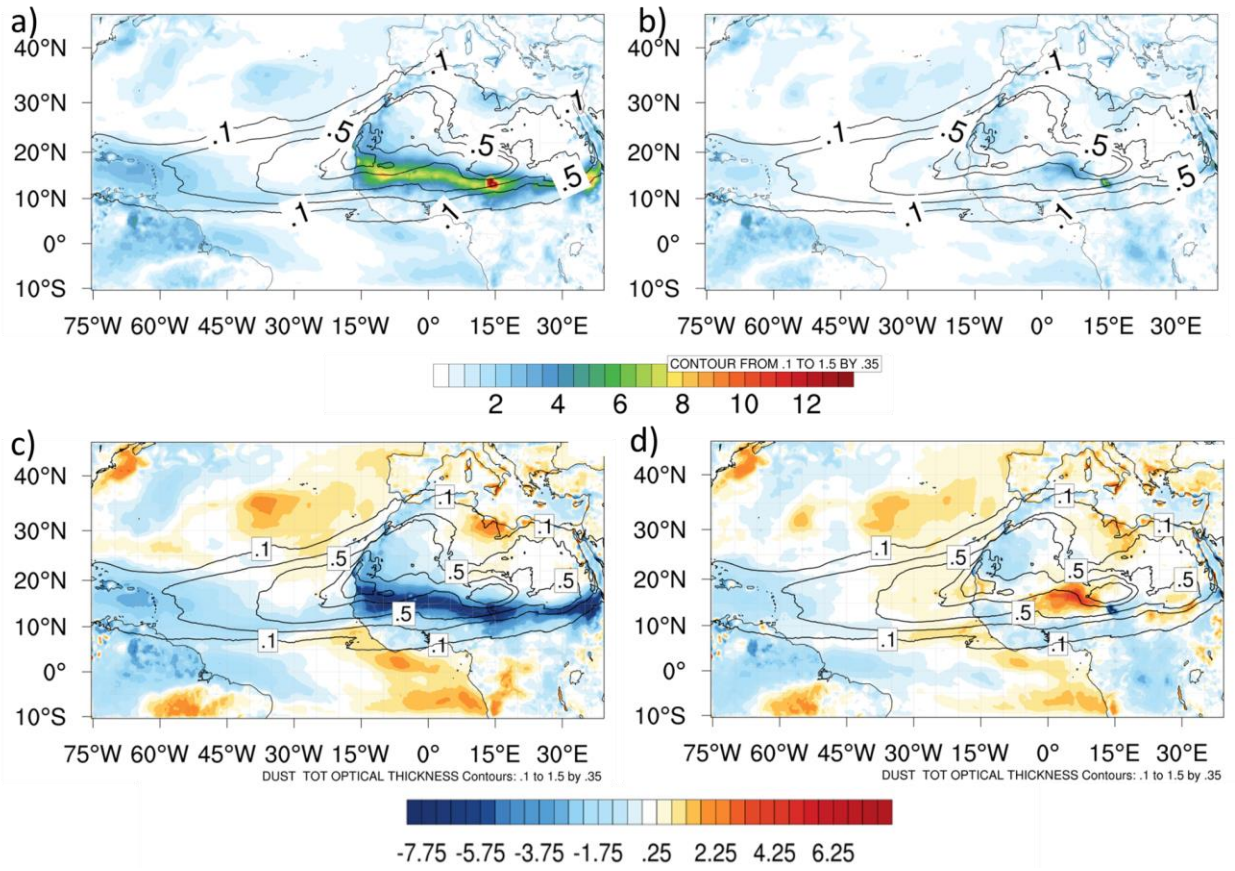

Figure 12. *The mean (a, b) bias and (c, d) RMSE of 2-m moisture for (left) DOFF and (right) DON against reanalysis data from 16 to 30 June 2020. The black contours are AOD from DON for reference.*

After the inclusion of the dust effects (DON), large 10-m wind biases and RMSEs are greatly reduced due to the correction of large-scale circulations by dust. Consistent with Chen et al. (2021), Figure 13 shows that the dust radiative heating in the atmosphere creates a low SLP anomaly with the maximum amplitude about 4 hPa over the land and 3 hPa over the ocean. This low SLP anomaly induces a counterclockwise (cyclonic) circulation anomaly in the northern hemisphere due to the gradient wind relation. These wind anomaly vectors turn toward the low pressure anomaly center by surface friction. The large negative (i.e., weaker) trade wind biases at southern

and southeastern branches of the subtropical high in DOFF are corrected by the northeasterly wind anomaly at the northwestern quadrant of the dust-induced cyclonic circulation anomaly. As a result, the maximum RMSE is reduced from 4.7 m/s to 0.8 m/s (by 83%) in this region (Figure 10d). Similarly, the overestimated northeasterly flow at ~ 9ºN over the ocean in DOFF (Figure 10a) is weakened by the southwesterly wind anomaly at the southwestern quadrant of the dust-induced cyclonic circulation anomaly (Figure 10b and Figure 13). The maximum RMSE over this region is reduced by 36% from 3.9 m/s to 2.5 m/s (Figure 10d). For the dipole-pattern wind bias over North Africa, the error is corrected by shifting the ITD northward (Figure 14a versus 14b) due to the dust-induced southwesterly wind anomaly at the southeastern quadrant of the dust-induced cyclonic circulation anomaly (Figure 13), which advances (strengthens, i.e., orange shading) southwesterly monsoonal flow forward and retreats (weakens, i.e., blue shading) northeasterly Harmattan flows backward (Figures 13b and 14). However, the positive wind bias between 5ºN to 10ºN over southern North Africa in DOFF remains (Figure 10a versus Figure 10b and Figure 10c versus Figure 10d).

With the dust effects, the bias and RMSE of the T2 are significantly reduced over North Africa. The dust radiative heating at low levels, mainly contributed by the dust-induced downward longwave radiation flux (Figure 15), corrects the large cold bias and RMSEs over the desert. The maximum RMSE is reduced by 91% from 6.1 K to 0.6 K, except at ~18ºN and 15ºE near the coast and the area of 20ºN to 30ºN and 5ºE to 20ºE (Figure 11a versus 11b and 11c versus 11d). However, additional warm biases are also introduced, one over the Chad and the other is along the coastal region in Western Sahara, most likely due to the overestimation of dust over these regions. The inclusion of the dust effects is also capable of correcting the warm bias south of the desert. The reasons are similar to those for 900-hPa temperature correction, i.e., the northward shift of ITD,

and attenuated downward shortwave radiation flux at low levels by dust and more vigorous deep convective clouds induced by dust. The maximum RMSE is reduced by ~82% from 6.4 K to 1.2 K in this region. Over the ocean, the dust slightly reduces the warm bias over the coastal region and the cold bias at the far downstream of the dust plume (9ºN to 20ºN and 45ºW to 75ºW). This is because of the dust-induced changes in air-sea interactions, including SST (Figure 16) and latent and sensible heat fluxes (LHF & SHF) changes, which have an impact on T2 and Q2. Note that SST, T2, Q2, and 10-m winds are tied together by surface LHF and SHF. The processes involved in dust-induced air-sea interaction changes include the enhancement of trade winds and thus upwelling along the northwestern coast of North African, the decrease of the upper-ocean mixed layer depth, the change of SST (Figure 16), and the change of 10-m winds due to negative SLP anomaly (Chen et al. 2021).

The dry bias band and Q2 RMSE at 13º N over land in DOFF is removed after inclusion of the dust effects in DON (Figure 12a and 12c versus 12b and 12d). This is because the southward shift of the ITD zone in DOFF is fixed in DON by the dust-induced southwesterly flow anomaly discussed earlier. The RMSE is reduced by 72 % from 15.2 g/ kg to 4.3 g/ kg. The dust, however, introduces new errors in Q2, such as the wet bias at ~15 ºN between 0ºE and 15ºE over the land. The precipitation is over-simulated in this region (figure not shown), which causes more evaporation and wet bias. Both the Q2 dry and wet biases over the ocean are slightly improved and this is because of the dust-induced SST, LHF, and SHF changes (Chen et al. 2021).

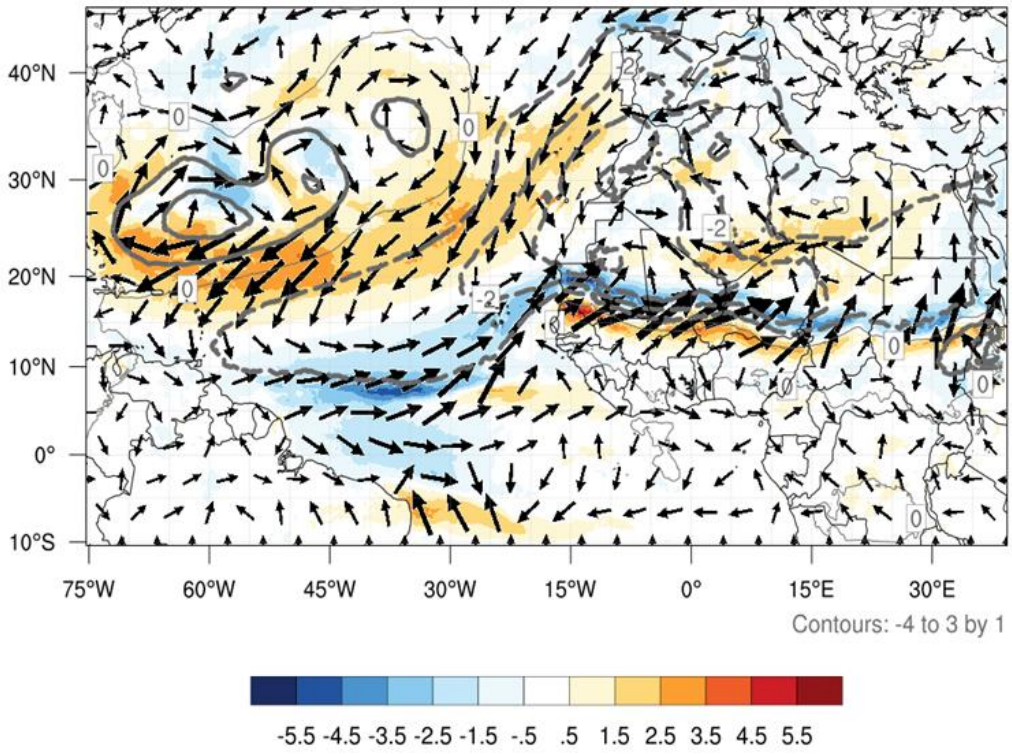

Figure 13. *The differences of 15-day mean SLP (hPa; gray contours) and 10-m wind speed (shading; m/s) and vector differences (thick arrows represent stronger speeds) between DON and DOFF (DON - DOFF). The solid gray lines are positive SLP differences and dashed lines are negative.*

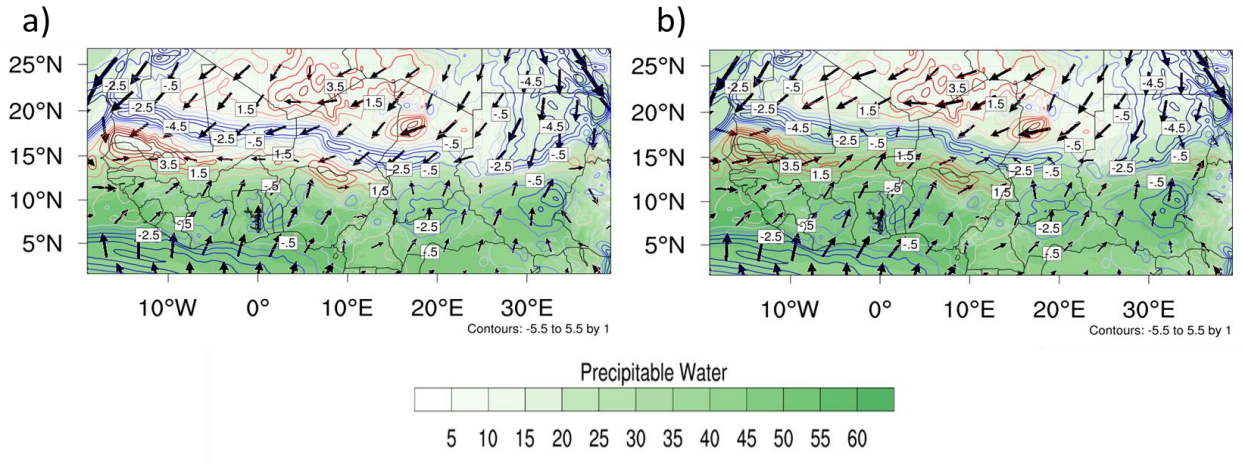

Figure 14. *The 15-day mean total precipitation water (mm; green shading) and 10-m wind vectors from (a) DOFF and (b) DON. Contours are wind speed differences between DON and DOFF (DON-DOFF) for reference. Blue contours are negative wind speed differences and red contours are positive wind speed differences. The black arrows are wind vectors.*

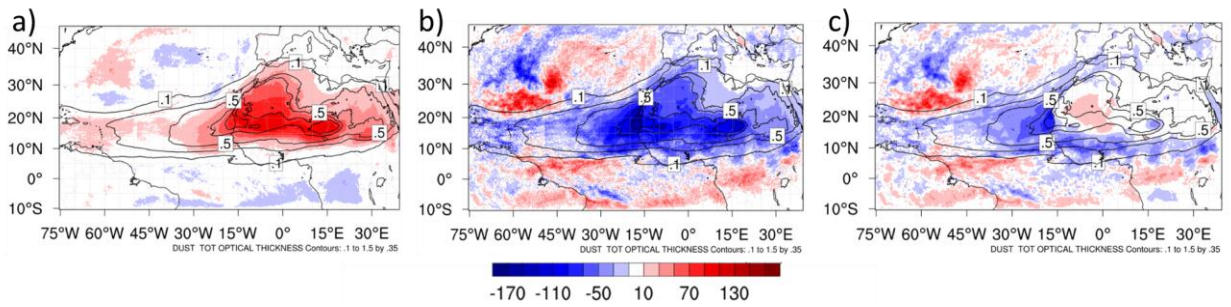

Figure 15. *The difference of 15-day mean radiation flux (W/m^2; DON-DOFF) from 16 to 30 June 2020 for (a) surface downward longwave radiation, (b) surface net downward shortwave radiation at surface, and (c) the summation of (a) and (b). The black contours are AOD from DON for reference.*

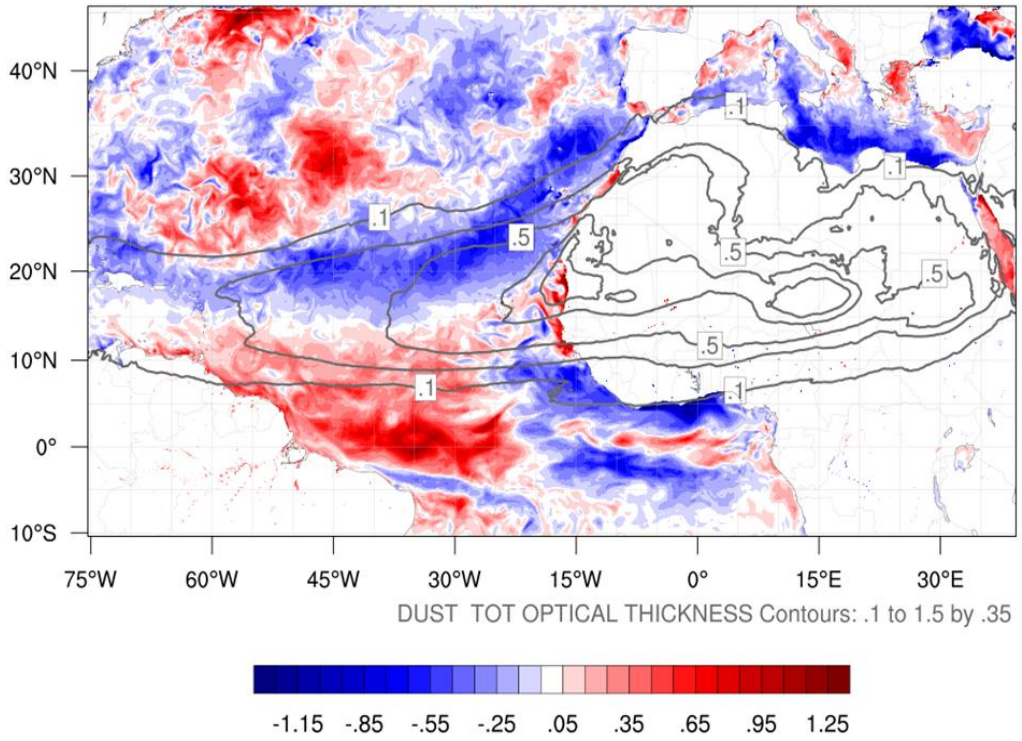

Figure 16. *The differences of 15-day mean sea surface temperature (K; color shading) from 16 to 30 June 2020 between DON and DOFF (DON – DOFF). The gray contours are AOD from DON for reference.*

3.3 Dust and cloud activities

As discussed in the introduction, dust can modulate cloud development through dust-radiation-cloud interactions and is examined here. Sensitivity experiments, such as turning off the

dust-radiation (DROFF) or the dust-cloud (DMOFF) interaction from the DON experiment, are performed to examine the role of individual dust processes in cloud development. Note that when we examine different processes, DON, which is again close to reality, is used as our reference. Our discussion will focus on cloud activities associated with the ITD, ITCZ and WAM.

Figures 17a and 17b show the 15-day averaged hydrometeors from DON and DOFF, respectively. The thick black contours in Figure 17 denote the primary precipitation region (> 40 mm during the 15-day period) in DON for reference. The maximum total hydrometeors are consistent with the rainfall region as expected, mainly contributed by convective cloud systems, located at 5ºN to 10ºN over the ocean and 8ºN to 13ºN over the land. Compared to DOFF, dust expands cloud activities to a wider coverage latitudinally; enhances cloud activities and extends clouds further north over North Africa by pushing the ITD zone northward; and shifts the ITCZ convection northward west of 25ºW over the ocean with the reduction in the maximum amount of hydrometeors (Figure 17c).

The comparison between the dust-radiation effect (DON - DMOFF; Figure 17d) and the dust-cloud effect (DON - DROFF; Figure 17e), using DON as the reference, indicates that both effects have non-negligible influences on these tropical convective cloud systems. Their influences on deep convective clouds over the ITCZ and the WAM regions are in general in phase, but the dust-radiation effect has a greater influence than the dust-cloud effect. This conclusion is consistent with that in Huang et al. (2019), which studies the dust-radiation versus dust-cloud effect on the development of an MCS over North Africa.

Outside the ITCZ, while the dust-radiation effect is the main contributor to the low-level cloud enhancement over the southern coastal region and the northward extension of monsoon cloud activities over West Africa, the dust-cloud effect often acts opposite (Figure 17d versus 17e). Why

are these clouds more active in DON than DOFF? This will be explored in the future. The averaged hydrometeors associated with these tropical cloud systems between 8ºN to 10ºN over West Africa is increased by 75% by dust during this 15-day period.

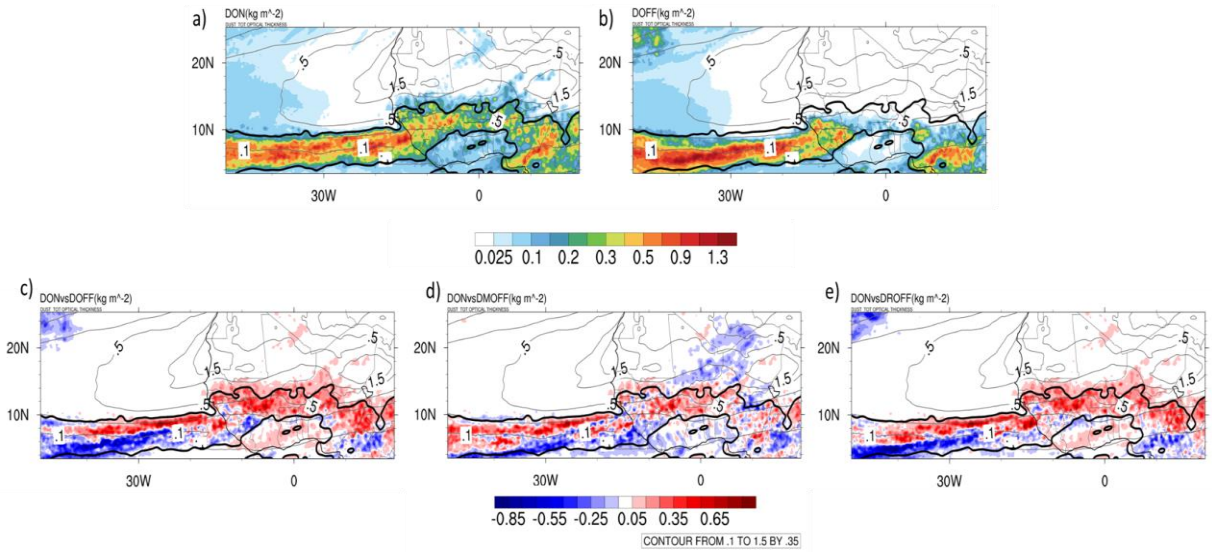

Figure 17. *The mean hydrometeors (shading; kg/m^2) from 16 to 30 June 2020 for (a) DON, and (b) DOFF. The difference of the mean hydrometeors from 16 to 30 June 2020 between (c) DON and DOFF (DON-DOFF). (d) and (e) are the same as (c) except for DON against from DMOFF and DON against from DROFF. The thick black contours represent the ITCZ rainfall location in DON.*

Why are the ITCZ and the ITD locations shifted northward by dust? While the reason has been covered in Section 3.2, we will briefly summarize it again here. A theory why ITCZ was shifted northward by dust has been proposed by Wilcox et al. (2010). They attributed it to the stronger vertical wind shear and the northward shift of AEJ by dust (see introduction). In this study, we provide another hypothesis that can explain the northward shift of both ITCZ and ITD. As discussed in Section 3.2, dust induces a negative SLP change with the maximum magnitude of ~4 hPa over the land. The low pressure anomaly results in a cyclonic convergence circulation anomaly near the surface (Figure 13). Over the ocean west of 25ºW where the ITCZ is shifted northward by dust, the dust-induced negative pressure anomaly and the resulting southwesterly flow anomaly

weaken the northeasterly trade winds over this region, shifting the convergence zone (i.e., ITCZ) northward. Similarly, the dust-induced southwesterly flow anomaly over 10°N to 20°N in North Africa explains why the ITD zone is pushed northward, which allows more moisture to reach north, and thus extends cloud activities further north into the desert.

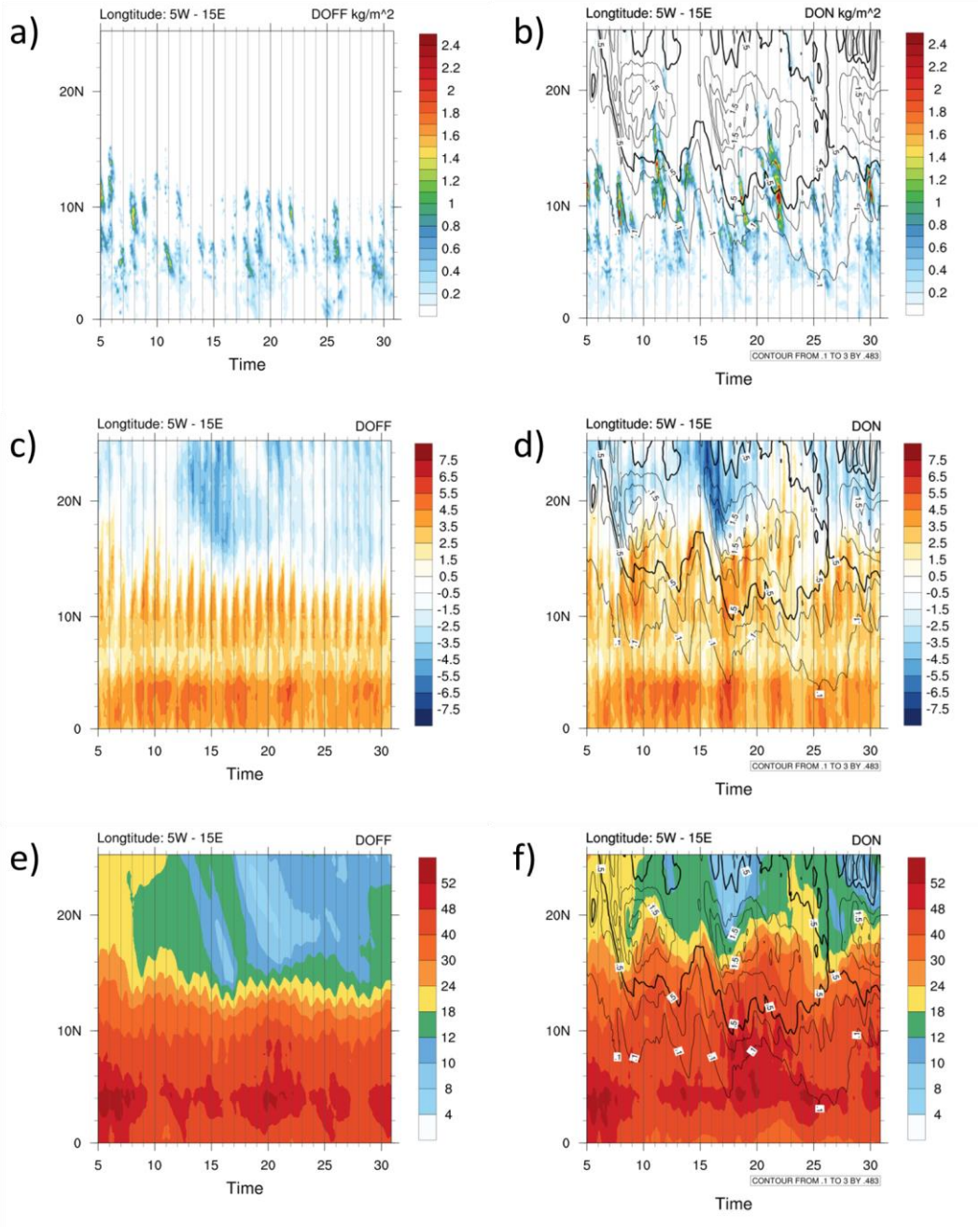

Figure 18. *The Hovmoller diagram of (a-b) hydrometeors (kg/m^2; shading), (c-d) V component of 10-m wind (V-wind; m/s), and (e-f) total precipitation water (TPW; mm) for (left) DOFF, and (right) DON from 5 to 30 June 2020. The black contours represent the AOD from DON.*

While the 15-day averaged result shows that dust can influence cloud activities over North Africa, time series data are further analyzed to explore their relation. Figure 18 shows the Hovmoller diagrams of column hydrometeors (kg/m^2), total precipitation water (TPW; mm), and the north-south component of 10-m wind (V-wind) for DOFF and DON from 5 to 30 June 2020. Note that since the land's response time to the dust effect is shorter than the ocean, data from 5 June is used in order to increase the sampling size.

Figure 18a shows that clouds in DOFF are often initiated at two latitude zones where convergence occurs. One is at ~ 6^{o}N due to the sea breeze, and the other is at ~12^{o}N, south of the ITD. The ITD is where the moist and dry air as well as southerly and northerly flow meet (Figure 18c). We note that only the southerly wind is shown at ~ 6^{o}N in Figure 18c. This is because the diurnal circulation is embedded in the southwesterly monsoonal flow. The clouds south of ITD are of our primary interest since these clouds are formed close to the dust source region. The latitudinal location of the ITD, whose feature is similar to the dryline in the Grant Plains, varies in time but in general is positioned at 14^{o}N. Once clouds (storms) are initiated at the northern edge of the moist air, they propagate southwestward (see the slope of the cloud trajectory). The characteristics of individual storms vary significantly but all show a strong diurnal signal. The clouds are less active when northerly winds at north of ITD become strong, which advect dry air southward. Consistent with clouds, the diurnal signal is also clearly shown in the V-wind (Figure 18c) and the northward transport of water vapor (Figure 18e). The maximum northward moisture intrusion occurred at 0900 UTC (the same as the local time), while clouds initiate at about 1200 UTC after

the surface receives more solar radiation. The clouds in general reach the maximum intensity at 1800 UTC.

Compared with DOFF, clouds in DON (Figure 18b) are more active and can develop further north, consistent with that shown in Figures 17a and 17b. These clouds are more intense and can have a longer life cycle. For example, the storm that developed from 21 to 23 June in DON propagated from 19ºN to 8ºN. The moving speed of the storm is about 6.64 m/s. The diurnal signal is still seen in the intensity change of these clouds. As expected, the development of these cloud systems are consistent with the further northward moisture intrusion by the V-wind.

There are three major dust events during the 25-day period, such as 07 to 13, 15 to 24, and 27 to 30 June (Figure 18b). As we discussed in section 3.2, the ITD is shifted northward, and clouds become more active once the dust effect is included. Here, we further examine how dust relates the northward moisture intrusion (or the enhancement of the V-wind) and cloud development. To do so, the time series of the meridionally averaged hydrometeors, V-wind, TPW and AOD between different latitudes (see the caption of Figure 19 for latitude information) in the Hovmoller diagrams (i.e., a box average) are plotted. Consistent with the earlier discussion, the variation of TPW at the ITD region is clearly correlated to the V-wind with a correlation coefficient of 0.66 for DOFF and 0.59 for DON, which are significant in both experiments (p-value ~0 for both DOFF and DON). The TPW value becomes larger (i.e., northward intrusion) as the V-wind increases, which transports more moisture northward. The correlation coefficient between AOD and V-wind is 0.52 after V-wind shifting 2 days and 9 hours, which is also significant (p-value ~ 0). With the moisture transported further northward, storms have a higher likelihood to develop in the north (see the histogram in Figure 19). The box-averaged V-wind (blue line) shows a stronger diurnal cycle but is also modulated by a lower frequency wave, which has a similar frequency as the dust events.

Note that the modulation of the diurnal cycle by a lower frequency wave is also seen in DOFF when the dust effect is excluded. In DON, there is a time shift between the V-wind and the AOD curves, with the AOD peak leading the V-wind peak from one to several days. In general, the box-averaged V-wind (blue line) weakens before the AOD peaks and then gradually intensifies after the AOD peak.

A schematic diagram that explains the relation between the V-wind variation and a dust plume is presented in Figure 20 to explain the peak shift between AOD and the V-wind over the ITD region. We note that this diagram is very idealized as the purpose is to illustrate the concept in a rather simple fashion. When a dust storm occurs, it will induce a low pressure anomaly mainly due to the radiative heating, and result in a cyclonic circulation anomaly. The dust plume transports westward following AEJ and passes the box area of interest (i.e., the red rectangular box in Figure 20). The box-averaged wind will be influenced by the dust plume when the plume passes through the region, and in general, this can be divided into three time periods: 1) before the center of the dust plume reaches the eastern boundary, 2) during the time when the dust plume center moves from the eastern boundary to the western boundary, and 3) after the plume center leaves the western boundary. *During the first time period*, when the dust plume moves into the box area through the eastern boundary (box-averaged AOD increasing), the northerly wind anomaly at the western side of the dust plume will arrive the box first and contribute to the box-averaged value, resulting in the decrease of the average V-wind until the dust plume center reaches the eastern side of the box (Figure 20a). When the dust plume center arrives at the eastern boundary, the northerly wind contribution reaches the maximum. *During the second time period*, when the dust plume center enters the box area (AOD continuing increasing), the box-averaged V-wind starts increasing. This is because the southerly wind anomaly at the eastern side of the dust plume starts contributing

to the average value until the entire dust plume is inside the box, or when the dust plume center reaches the center of the box if the dust plume size is larger than the box (Figure 20b). *During the third time period*, once the western edge of the dust plume starts departing from the box (AOD decreasing), the contribution of the southerly wind anomaly (i.e., the eastern side of the dust plume) becomes dominant and the V-wind will increase until the dust plume moves out of the box (Figure 20c). This briefly explains why there is a shift between the dust plume and the V-wind peaks in Figure 19b.

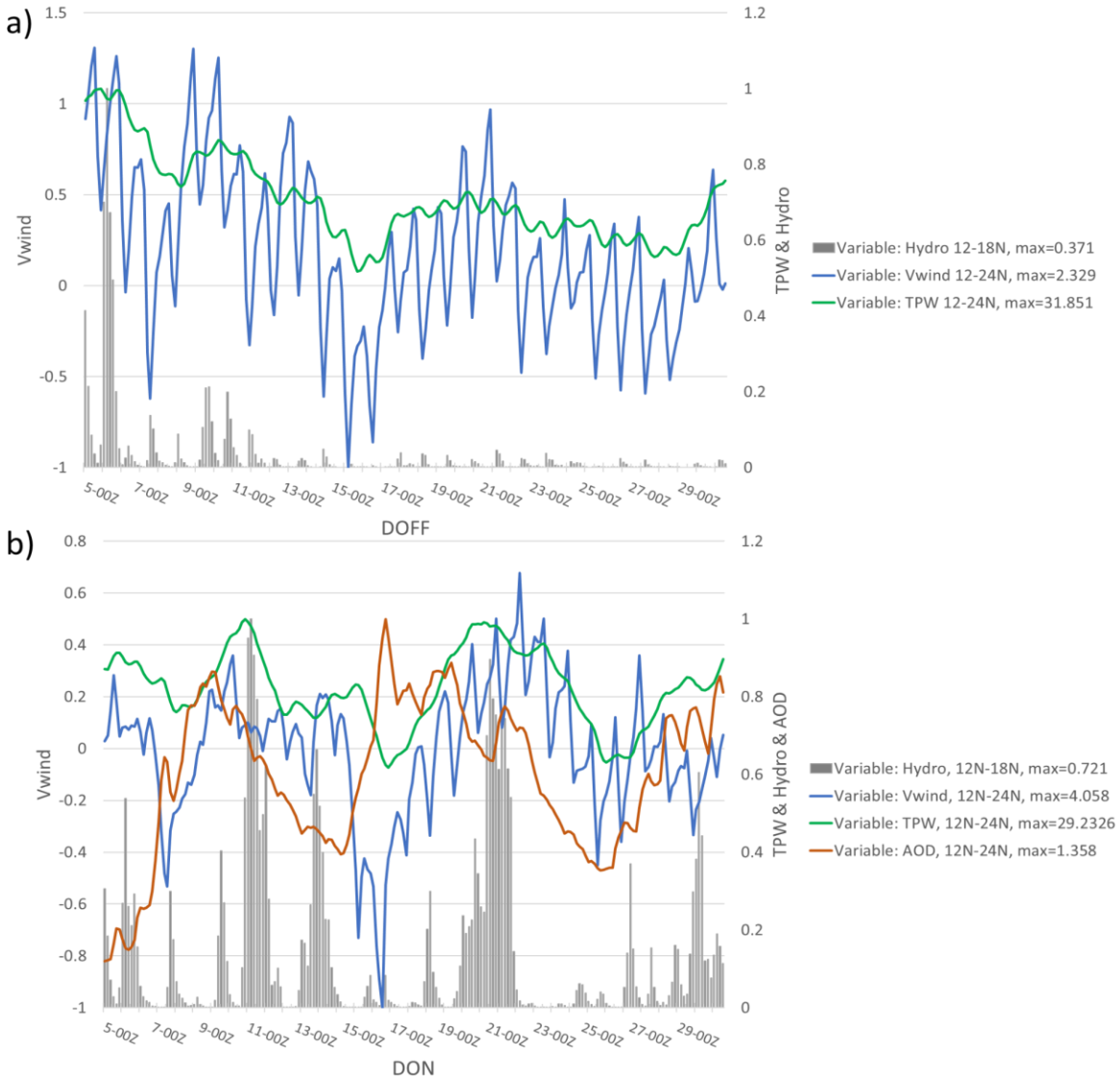

Figure 19. *The schematic diagram for (top) DOFF and (bottom) DON. The gray histogram represents hydrometeors. The blue line represents V-wind. The green line represents TPW. The orange line represents AOD. The box average of longitude is 5ºW to 15ºE and the latitude information for each variable are shown in the figures.*

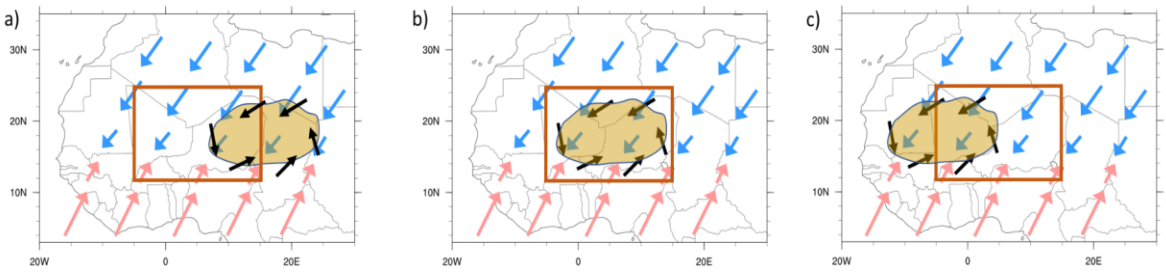

Figure 20. *The schematic diagram of wind changes over the ITD zone when a dust plume passes the box in interest. The light blue arrows represent the northeasterly flow. The pink arrows represent southwesterly flow. The brown box is the same as Figure 20. The total winds will be adding the dust-induced wind (black arrows) to the background winds (i.e., blue and pink arrows).*

3. Summary and concluding remarks

The Sahara Desert emits the largest amount of dust in the world (Querol et al., 2019) and the dust can be transported westward eventually reaching the United States. Observations and numerical studies have shown that the dust-cloud-radiation interactions play an important role in modulating large-scale circulations and weather and climate systems, in particular those near the dust source regions. However, none of them provide thorough quantitative error analysis on how dust can influence the model performance. Chen et al. (2021) investigated the influence of Saharan dust on air-sea interactions over the Tropical North Atlantic Ocean. This study, which is an extended work from Chen et al. (2021), focuses on quantifying the improvement of meteorological variables by dust and interpreting how dust modulates large-scale circulations, which in turn reduce modeled meteorological variable errors over North Africa and the Eastern Atlantic Ocean. The mean bias and root mean square error (RMSE) are used to quantify error characteristics. In addition, the influence of dust on cloud activities over these regions is also investigated.

The fully coupled WRF-ROMS-DUST (WRD) model is used to carry out numerical simulations. Two experiments were conducted. They are identical except that one activated the dust-radiation-cloud interactions (DON) and the other did not (DOFF). In addition, to examine the role of individual dust physical processes in cloud development, two sensitivity experiments were performed, one turning off the dust-radiation interaction (DROFF) and the other turning off the dust-cloud interaction (DMOFF) from the DON experiment. Two domains were used. The parent domain is 12 km and the child domain is 4 km. The model integrated for one month starting from 1 June 2020, and only the last 15-day data were used for analysis. The physics schemes used in model simulations include the two-moment microphysics scheme (Cheng et al., 2010; Huang et al., 2019), the FLG radiation scheme (Gu et al., 2010, 2011), the KF cumulus scheme (Kain, 2004) and the MRF boundary layer scheme (Hong & Pan, 1996). The cumulus parameterization was only applied to domain 1. For the ocean, the GLS vertical mixing scheme was used (Umlauf & Burchard, 2003). The computational time is more costly than that in Chen et al., 2021 (more than 50 hours for 1-month simulation using 3200 cores).

In general, the model reasonably produces the observed AOD pattern and magnitude, but the values are slightly overestimated. The simulated meteorological variables between DON and DOFF are compared and evaluated against FNL reanalysis. There is a strong cold bias over the northwestern half of the desert from the surface to the 750-hPa or higher up in DOFF. In DON, because of the dust radiative heating, the cold bias at 750 hPa is almost removed, and the maximum RMSE of the 750-hPa temperature located at (~ 26ºN, 1ºW) is reduced by dust by 91% from 4.6 K to 0.4 K. The maximum RMSE of the 900-hPa temperature over the desert is also reduced by dust by 92% from 4.8 K to 0.4 K. The improvement of the temperature is mainly due to the dust-shortwave radiation interaction at the middle levels and the dust-longwave radiation interaction at

lower levels. Unfortunately, the dust also creates new errors such as the warm bias over the coastal region and the maximum RMSE is almost doubled by dust (~ 4.2 K).

For 650-hPa AEJ, after including the dust-cloud-radiation interactions, the jet is enhanced, extended westward, and shifted northward. The maximum RMSE is reduced by 90% over the major error regions east of 35ºW. The correction of the AEJ is mainly due to the gradient of the dust heating via the thermal wind relation.

Near the surface, the dust radiative heating generates a low SLP anomaly under the dust plume region. The anomaly is about 4 hPa over the desert and 3 hPa over the ocean. The low SLP anomaly induces a cyclonic circulation anomaly, which deflects toward the dust plume center due to the surface friction. The cyclonic circulation anomaly corrects the major 10-m wind errors and RMSEs at different regions. The trade winds at the south and southwestern branches of the subtropical high are greatly improved by dust as they are too weak in DOFF. The maximum RMSE of the 10-m wind is reduced by 83% over this region. In addition, both the ITD and the ITCZ are shifted to the north by the strengthened southwesterly monsoonal flow over the southern side of the dust plume. The mechanism proposed here in fact is different from what was proposed in Wilcox, et al. (2010).

Due to the downward dust-longwave radiation flux, convective cloud changes, and the correction of the ITD location, the maximum RMSE of the 2-m temperature is reduced by 91% over the desert. Likewise, the RMSE of 2-m moisture is fixed by the shifting of ITCZ and ITD, and the maximum error is reduced by 72%.

Comparing DROFF and DMOFF with DON, both the dust-radiation and dust-cloud effects have important and positive (i.e., more active) influences on ITCZ convective cloud development,

and their influences are in phase. However, the dust-radiation effect has a greater impact than the dust-cloud effect, similar to what was found in Huang et al. (2019). The dust-radiation effect is the dominant process for the northward extension of monsoon cloud activities over North West Africa. While the dust-cloud effect plays a minor role in these clouds, it is often opposite to the dust-radiation effect.

The correlations between dust, V-wind and northward moisture transport over the ITD region were studied. The variation of TPW over the ITD region is correlated to the V-wind with a correlation coefficient of 0.66 for DOFF and 0.59 for DON, and they both are statistically significant (p-value ~ 0). There is a phase shift between the AOD and V-wind, and their correlation coefficient is 0.52 after V-wind shifting 2 days and 9 hrs., and their relation is also statistically significant (p-values ~0).

The northerly flow and southerly flow in the ITD region can be modulated by individual dust plumes when they propagate westward. This is because of the dust-induced cyclonic circulation mainly due to the dust radiative effect. Over the region of (12ºN to 24ºN and l5ºW to 15ºE), where convective storms are often initiated at the northern edge of the southwesterly monsoonal flow, the averaged V-wind over the region will decrease (i.e., more northerly flow) as the dust plume enters the region and increase (i.e., more southerly flow) as the dust plume exits the region.

This study shows that while the dust can significantly reduce biases and RMSEs of meteorological variables over North Africa and the Eastern Atlantic Ocean, it also introduces new errors at different locations. This is mainly due to the errors in dust parametrizations (dust sizes, dust emission, etc.), in addition to other model errors. Moreover, the dust tends to settle too fast over the middle and western Atlantic Ocean after long-range transport. Thus, further

improvements on dust parameterizations in the WRD model, such as dust size distribution, dust-radiation interactions, etc., are needed in order to reduce the appearance of new errors. Finally, we would like to point out that the conclusions drawn from the study are based only on one-month simulations. A seasonal or multi-seasonal study will be needed, and this will be conducted in the future.

References

Bangalath, H. K., & Stenchikov, G. (2015). Role of dust direct radiative effect on the tropical rain belt over Middle East and North Africa: A high-resolution AGCM study: DUST RADIATIVE EFFECT OVER MENA. *Journal of Geophysical Research: Atmospheres*, *120*(10), 4564–4584. https://doi.org/10.1002/2015JD023122

Bercos-Hickey, E., Nathan, T. R., & Chen, S. H. (2017). Saharan dust and the African easterly jet–African easterly wave system: Structure, location and energetics. *Quarterly Journal of the Royal Meteorological Society*, *143*(708), 2797–2808. https://doi.org/10.1002/qj.3128

Bercos-Hickey, E., Nathan, T. R., & Chen, S.-H. (2020). On the Relationship between the African Easterly Jet, Saharan Mineral Dust Aerosols, and West African Precipitation. *Journal of Climate*, *33*(9), 3533–3546. https://doi.org/10.1175/JCLI-D-18-0661.1

Chen, J. P., Tsai, I. C., & Lin, Y. C. (2013). A statistical-numerical aerosol parameterization scheme. *Atmospheric Chemistry and Physics*, *13*(20), 10483–10504. https://doi.org/10.5194/acp-13-10483-2013

Chen, J.-P., Hazra, A., & Levin, Z. (2008). Atmospheric Chemistry and Physics Parameterizing ice nucleation rates using contact angle and activation energy derived from laboratory data. In *Atmos. Chem. Phys* (Vol. 8, pp. 7431–7449). www.atmos-chem-phys.net/8/7431/2008/

Chen, S. H., Huang, C. C., Kuo, Y. C., Tseng, Y. H., Gu, Y., Earl, K., Chen, C. Y., Choi, Y., & Liou, K. N. (2021). Impacts of Saharan Mineral Dust on Air-Sea Interaction over North Atlantic Ocean Using a Fully Coupled Regional Model. *Journal of Geophysical*

Research: Atmospheres, *126*(4). https://doi.org/10.1029/2020JD033586

Chen, S. H., Wang, S. H., & Waylonis, M. (2010). Modification of Saharan air layer and environmental shear over the eastern Atlantic Ocean by dust-radiation effects. *Journal of Geophysical Research Atmospheres*, *115*(21). https://doi.org/10.1029/2010JD014158

Chen, S.-H., Liu, Y.-C., Nathan, T. R., Davis, C., Torn, R., Sowa, N., Cheng, C.-T., & Chen, J.-P. (2015). Modeling the effects of dust-radiative forcing on the movement of Hurricane *Helene* (2006): Effect of Dust-Radiative Forcing on *Helene* Movement. *Quarterly Journal of the Royal Meteorological Society*, *141*(692), 2563–2570. https://doi.org/10.1002/qj.2542

Cheng, C. T., Wang, W. C., & Chen, J. P. (2010). Simulation of the effects of increasing cloud condensation nuclei on mixed-phase clouds and precipitation of a front system. *Atmospheric Research*, *96*(2–3), 461–476. https://doi.org/10.1016/j.atmosres.2010.02.005

Choobari, O. A., Zawar-Reza, P., & Sturman, A. (2014). The global distribution of mineral dust and its impacts on the climate system: A review. *Atmospheric Research*, *138*, 152–165. https://doi.org/10.1016/j.atmosres.2013.11.007

DeMott, P. J., Rogers, D. C., Kreidenweis, S. M., Chen, Y., Twohy, C. H., Baumgardner, D., Heymsfield, A. J., & Chan, K. R. (1998). The role of heterogeneous freezing nucleation in upper tropospheric clouds: Inferences from SUCCESS. *Geophysical Research Letters*, *25*(9), 1387–1390. https://doi.org/10.1029/97GL03779

Dunion, J. P., & Velden, C. S. (2004). The Impact of the Saharan Air Layer on Atlantic Tropical Cyclone Activity. *Bulletin of the American Meteorological Society*, *85*(3), 353–366. https://doi.org/10.1175/BAMS-85-3-353

Evan, A. T., Heidinger, A. K., Bennartz, R., Bennington, V., Mahowald, N. M., Corrada-Bravo,

H., Velden, C. S., Myhre, G., & Kossin, J. P. (2008). Ocean temperature forcing by aerosols across the Atlantic tropical cyclone development region. *Geochemistry, Geophysics, Geosystems*, *9*(5). https://doi.org/10.1029/2007GC001774

Evans, S., Dawson, E., & Ginoux, P. (2020). Linear Relation Between Shifting ITCZ and Dust Hemispheric Asymmetry. *Geophysical Research Letters*, *47*(22). https://doi.org/10.1029/2020GL090499

Fan, J., Yuan, T., Comstock, J. M., Ghan, S., Khain, A., Leung, L. R., Li, Z., Martins, V. J., & Ovchinnikov, M. (2009). Dominant role by vertical wind shear in regulating aerosol effects on deep convective clouds. *Journal of Geophysical Research Atmospheres*, *114*(22). https://doi.org/10.1029/2009JD012352

Field, P. R., Mohler, O., Connolly, P., Kramer, M., Cotton, R., Heymsfield, A. J., Saathoff, H., & Schnaiter, M. (2006). Some ice nucleation characteristics of Asian and Saharan desert dust. *Atmos. Chem. Phys.*, 16, 2991–3006, https://doi.org/10.5194/acp-6-2991-2006, 2006.

Gettelman, A., & Morrison, H. (2015). Advanced two-moment bulk microphysics for global models. Part I: Off-line tests and comparison with other schemes. *Journal of Climate*, *28*(3), 1268–1287. https://doi.org/10.1175/JCLI-D-14-00102.1

Grogan, D. F. P., Nathan, T. R., & Chen, S.-H. (2016). Effects of Saharan Dust on the Linear Dynamics of African Easterly Waves. *Journal of the Atmospheric Sciences*, *73*(2), 891–911. https://doi.org/10.1175/JAS-D-15-0143.1

Grogan, D. F. P., Nathan, T. R., & Chen, S.-H. (2019). Structural Changes in the African Easterly Jet and Its Role in Mediating the Effects of Saharan Dust on the Linear Dynamics of African Easterly Waves. *Journal of the Atmospheric Sciences*, *76*(11),

3351–3365. https://doi.org/10.1175/JAS-D-19-0104.1

Gu, Y., Liou, K. N., Chen, W., & Liao, H. (2010). Direct climate effect of black carbon in China and its impact on dust storms. *Journal of Geophysical Research*, *115*. https://doi.org/10.1029/2009jd013427

Gu, Y., Liou, K. N., Ou, S. C., & Fovell, R. (2011). Cirrus cloud simulations using WRF with improved radiation parameterization and increased vertical resolution. *Journal of Geophysical Research Atmospheres*, *116*(6). https://doi.org/10.1029/2010JD014574

Hong, S.-Y., & Pan, H.-L. (1996). *Nonlocal Boundary Layer Vertical Diffusion in a Medium-Range Forecast Model*. 2322–2339. https://doi.org/10.1175/1520-0493(1996)124<2322:NBLVDI>2.0.CO;2

Hong, S.-Y., Noh, Y., & Dudhia, J. (2006). A New Vertical Diffusion Package with an Explicit Treatment of Entrainment Processes. Monthly Weather Review, 134(9), 2318–2341. https://doi.org/10.1175/MWR3199.1

Hoose, C., Kristjánsson, J. E., Chen, J. P., & Hazra, A. (2010). A classical-theory-based parameterization of heterogeneous ice nucleation by mineral dust, soot, and biological particles in a global climate model. *Journal of the Atmospheric Sciences*, *67*(8), 2483–2503. https://doi.org/10.1175/2010JAS3425.1

Huang, C.-C., Chen, S.-H., Lin, Y.-C., Earl, K., Matsui, T., Lee, H.-H., Tsai, I.-C., Chen, J.-P., & Cheng, C.-T. (2019). Impacts of Dust–Radiation versus Dust–Cloud Interactions on the Development of a Modeled Mesoscale Convective System over North Africa. *Monthly Weather Review*, *147*(9), 3301–3326. https://doi.org/10.1175/MWR-D-18-0459.1

Jordan, A. K., Gnanadesikan, A., & Zaitchik, B. (2018). Simulated Dust Aerosol Impacts on Western Sahelian Rainfall: Importance of Ocean Coupling. *Journal of Climate*, *31*(22),

9107–9124. https://doi.org/10.1175/JCLI-D-17-0819.1

Kain, J. S. (2004). The Kain-Fritsch Convective Parameterization: An Update. *Journal of Applied Meteorology*, *43*(1), 170–181. https://doi.org/10.1175/1520-0450(2004)043<0170:TKCPAU>2.0.CO;2

Karydis, V. A., Kumar, P., Barahona, D., Sokolik, I. N., & Nenes, A. (2011). On the effect of dust particles on global cloud condensation nuclei and cloud droplet number: DUST IMPACTS ON CLOUD CONDENSATION NUCLEI. *Journal of Geophysical Research: Atmospheres*, *116*(D23), n/a-n/a. https://doi.org/10.1029/2011JD016283

Koehler, K. A., Kreidenweis, S. M., DeMott, P. J., Petters, M. D., Prenni, A. J., & Carrico, C. M. (2009). Hygroscopicity and cloud droplet activation of mineral dust aerosol. *Geophysical Research Letters*, *36*(8). https://doi.org/10.1029/2009GL037348

Kumar, P., Sokolik, I. N., & Nenes, A. (2011a). Cloud condensation nuclei activity and droplet activation kinetics of wet processed regional dust samples and minerals. *Atmospheric Chemistry and Physics*, *11*(16), 8661–8676. https://doi.org/10.5194/acp-11-8661-2011

Kumar, P., Sokolik, I. N., & Nenes, A. (2011b). Measurements of cloud condensation nuclei activity and droplet activation kinetics of fresh unprocessed regional dust samples and minerals. *Atmospheric Chemistry and Physics*, *11*(7), 3527–3541. https://doi.org/10.5194/acp-11-3527-2011

Liu, W., Cook, K. H., & Vizy, E. K. (2019). The role of mesoscale convective systems in the diurnal cycle of rainfall and its seasonality over sub-Saharan Northern Africa. *Climate Dynamics*, *52*(1–2), 729–745. https://doi.org/10.1007/s00382-018-4162-y

Martínez, I. R., & Chaboureau, J.-P. (2018). Precipitation and Mesoscale Convective Systems: Radiative Impact of Dust over Northern Africa. *Monthly Weather Review*, *146*(9), 3011–

3029. https://doi.org/10.1175/MWR-D-18-0103.1

Nathan, T. R., Grogan, D. F. P., & Chen, S.-H. (2017). Subcritical Destabilization of African Easterly Waves by Saharan Mineral Dust. *Journal of the Atmospheric Sciences*, *74*(4), 1039–1055. https://doi.org/10.1175/JAS-D-16-0247.1

Nathan, T. R., Grogan, D. F. P., & Chen, S.-H. (2019). Saharan Dust Transport during the Incipient Growth Phase of African Easterly Waves. *Geosciences*, *9*(9), 388. https://doi.org/10.3390/geosciences9090388

Navea, J. G., Chen, H., Huang, M., Carmichel, G. R., & Grassian, V. H. (2010). A comparative evaluation of water uptake on several mineral dust sources. *Environmental Chemistry*, *7*(2), 162–170. https://doi.org/10.1071/EN09122

Nicholson, S. E. (2009). A revised picture of the structure of the "monsoon" and land ITCZ over West Africa. *Climate Dynamics*, *32*(7–8), 1155–1171. https://doi.org/10.1007/s00382-008-0514-3

Paukert, M., Hoose, C., & Simmel, M. (2017). Redistribution of ice nuclei between cloud and rain droplets: Parameterization and application to deep convective clouds. *Journal of Advances in Modeling Earth Systems*, *9*(1), 514–535. https://doi.org/10.1002/2016MS000841

Pérez, C., Nickovic, S., Pejanovic, G., Baldasano, J. M., & Özsoy, E. (2006). Interactive dust-radiation modeling: A step to improve weather forecasts. *Journal of Geophysical Research Atmospheres*, *111*(16). https://doi.org/10.1029/2005JD006717

Querol, X., Tobías, A., Pérez, N., Karanasiou, A., Amato, F., Stafoggia, M., Pérez García-Pando, C., Ginoux, P., Forastiere, F., Gumy, S., Mudu, P., & Alastuey, A. (2019). Monitoring the impact of desert dust outbreaks for air quality for health studies. *Environment*

International, *130*, 104867. https://doi.org/10.1016/j.envint.2019.05.061

Romakkaniemi, S., Arola, A., Kokkola, H., Birmili, W., Tuch, T., Kerminen, V.-M., Räisänen, P., Smith, J. N., Korhonen, H., & Laaksonen, A. (2012). Effect of aerosol size distribution changes on AOD, CCN and cloud droplet concentration: Case studies from Erfurt and Melpitz, Germany: AEROSOL EFFECT ON AOD AND CLOUDS. *Journal of Geophysical Research: Atmospheres*, *117*(D7), n/a-n/a. https://doi.org/10.1029/2011JD017091

Ross, K. E., Piketh, S. J., Bruintjes, R. T., Burger, R. P., Swap, R. J., & Annegarn, H. J. (2003). Spatial and seasonal variations in CCN distribution and the aerosol-CCN relationship over southern Africa: CCN DISTRIBUTION AND THE AEROSOL-CCN RELATIONSHIP. *Journal of Geophysical Research: Atmospheres*, *108*(D13), n/a-n/a. https://doi.org/10.1029/2002JD002384

Schwendike, J., & Jones, S. C. (2010). Convection in an African easterly wave over West Africa and the eastern Atlantic: A model case study of Helene (2006). *Quarterly Journal of the Royal Meteorological Society*, *136*(SUPPL. 1), 364–396. https://doi.org/10.1002/qj.566

Shchepetkin, A. F., & McWilliams, J. C. (2005). The regional oceanic modeling system (ROMS): A split-explicit, free-surface, topography-following-coordinate oceanic model. *Ocean Modelling*, *9*(4), 347–404. https://doi.org/10.1016/j.ocemod.2004.08.002

Shi, J. J., Matsui, T., Tao, W. K., Tan, Q., Peters-Lidard, C., Chin, M., Pickering, K., Guy, N., Lang, S., & Kemp, E. M. (2014). Implementation of an aerosol-cloud-microphysics-radiation coupling into the NASA unified WRF: Simulation results for the 6-7 August 2006 AMMA special observing period. *Quarterly Journal of the Royal Meteorological Society*, *140*(684), 2158–2175. https://doi.org/10.1002/qj.2286

Skamarock, W. C., Klemp, J. B., Dudhia, J., Gill, D. O., Barker, D. M., Duda, M. G., Huang, X.-Y., Wang, W., & Powers, J. G. (2008). *A Description of the Advanced Research WRF Version 3*.

Strong, J. D. O., Vecchi, G. A., & Ginoux, P. (2015). The Response of the Tropical Atlantic and West African Climate to Saharan Dust in a Fully Coupled GCM. *Journal of Climate*, *28*(18), 7071–7092. https://doi.org/10.1175/JCLI-D-14-00797.1

Umlauf, L., & Burchard, H. (2003). A generic length-scale equation for geophysical turbulence models. *Journal of Marine Research*, 61, 235–265. https://doi.org/10.1357/002224003322005087

Warner, J. C., Armstrong, B., He, R., & Zambon, J. B. (2010). Development of a Coupled Ocean-Atmosphere-Wave-Sediment Transport (COAWST) Modeling System. *Ocean Modelling*, *35*(3), 230–244. https://doi.org/10.1016/j.ocemod.2010.07.010

Warner, J. C., Sherwood, C. R., Signell, R. P., Harris, C. K., & Arango, H. G. (2008). Development of a three-dimensional, regional, coupled wave, current, and sediment-transport model. *Computers and Geosciences*, *34*(10), 1284–1306. https://doi.org/10.1016/j.cageo.2008.02.012

Wilcox, E. M., Lau, K. M., & Kim, K.-M. (2010). A northward shift of the North Atlantic Ocean Intertropical Convergence Zone in response to summertime Saharan dust outbreaks: SAHARAN DUST OUTBREAKS AND ATLANTIC ITCZ. *Geophysical Research Letters*, *37*(4). https://doi.org/10.1029/2009GL041774

Zhang, H., McFarquhar, G. M., Saleeby, S. M., & Cotton, W. R. (2007). Impacts of Saharan dust as CCN on the evolution of an idealized tropical cyclone. *Geophysical Research Letters*, *34*(14), L14812. https://doi.org/10.1029/2007GL029876

Zhao, C., Liu, X., Ruby Leung, L., & Hagos, S. (2011). Radiative impact of mineral dust on monsoon precipitation variability over West Africa. *Atmospheric Chemistry and Physics*, *11*(5), 1879–1893. https://doi.org/10.5194/acp-11-1879-2011